OXFORD

Analogous cortical reorganization accompanies entry into states of reduced consciousness during anesthesia and sleep

Bryan M. Krause[1], Declan I. Campbell[1], Christopher K. Kovach[2], Rashmi N. Mueller[2,3], Hiroto Kawasaki[2], Kirill V. Nourski[2,4], Matthew I. Banks[1,5,*]

[1]Department of Anesthesiology, University of Wisconsin, Madison, WI, United States,
[2]Department of Neurosurgery, The University of Iowa, Iowa City, IA 52242, United States,
[3]Department of Anesthesia, The University of Iowa, Iowa City, IA 52242, United States,
[4]Iowa Neuroscience Institute, The University of Iowa, Iowa City, IA 52242, United States,
[5]Department of Neuroscience, University of Wisconsin, Madison, WI 53706, United States

*Corresponding author: Department of Anesthesiology, University of Wisconsin, 1300 University Avenue, Room 4605, Madison, WI 53706, United States. Email: mibanks@wisc.edu

Theories of consciousness suggest that brain mechanisms underlying transitions into and out of unconsciousness are conserved no matter the context or precipitating conditions. We compared signatures of these mechanisms using intracranial electroencephalography in neurosurgical patients during propofol anesthesia and overnight sleep and found strikingly similar reorganization of human cortical networks. We computed the "effective dimensionality" of the normalized resting state functional connectivity matrix to quantify network complexity. Effective dimensionality decreased during stages of reduced consciousness (anesthesia unresponsiveness, N2 and N3 sleep). These changes were not region-specific, suggesting global network reorganization. When connectivity data were embedded into a low-dimensional space in which proximity represents functional similarity, we observed greater distances between brain regions during stages of reduced consciousness, and individual recording sites became closer to their nearest neighbors. These changes corresponded to decreased differentiation and functional integration and correlated with decreases in effective dimensionality. This network reorganization constitutes a neural signature of states of reduced consciousness that is common to anesthesia and sleep. These results establish a framework for understanding the neural correlates of consciousness and for practical evaluation of loss and recovery of consciousness.

Key words: functional connectivity; intracranial electroencephalography; electrocorticography; electrophysiology; cortical networks.

Introduction

Consciousness is inextricably tied to the organizational structure of brain networks (Tononi et al. 2016; Mashour et al. 2020). Investigations into the neural correlates of consciousness suggest that changes in the brain underlying loss and recovery of consciousness (LOC, ROC) should overlap regardless of the circumstances, or contexts, of their occurrence (Alkire et al. 2008; Mashour and Hudetz 2018). LOC and ROC are likely precipitated by large-scale reorganization of cortical networks. This reorganization might result in altered functional integration and differentiation in the brain (Tononi et al. 2016), communication into or out of prefrontal cortex and amplification of sensory signals (Dehaene and Changeux 2011), or feedback connectivity (Mashour 2014) with concomitant effects on predictive processing (Bastos et al. 2012). Identifying the neural correlates of LOC and ROC remains a central goal of neuroscience research.

Comparing consciousness-related changes in brain networks across contexts facilitates identification of neural correlates that are specific to LOC and ROC. Two contexts of interest that are readily amenable to experimental investigation are general anesthesia and sleep. General anesthesia and sleep exhibit common behavioral and physiological features (Scheinin et al. 2021). Unconsciousness and dreaming (i.e. conscious experience while

disconnected from the environment) occur in both settings (Eer et al. 2009; Leslie et al. 2009; Siclari et al. 2013), as do decreased cerebral blood flow and metabolic rate (Hudetz 2012; Aalling et al. 2018; Elvsåshagen et al. 2019) and increased slow wave activity (Murphy et al. 2011). However, sleep and anesthesia are also clearly distinct. Patients are not as arousable during anesthesia compared to sleep, and the internal architecture of sleep, with its distinct and predictable stages, is not observed during anesthesia. Changes in brain network organization have been investigated during general anesthesia or sleep separately (Alkire et al. 2008; Mashour and Hudetz 2018), but in the small number of studies involving a direct comparison (Murphy et al. 2011; Li et al. 2018; Wang et al. 2020), no clear and consistent neural correlates have emerged. Thus, the degree to which the brain traverses an overlapping complement of network states during anesthesia versus sleep is still a matter of debate (Akeju and Brown 2017; Li et al. 2018; Sleigh et al. 2018).

The reorganization of cortical networks underlying LOC and ROC cannot be explained solely by changes in the magnitude of connectivity. For example, reports of changes in connectivity during anesthesia and sleep are inconsistent; some studies report that connectivity is decreased (Spoormaker et al. 2010; Boly et al. 2012a; Lee et al. 2013; Monti et al. 2013; Palanca et al. 2015;

Ranft et al. 2016; Sarasso et al. 2021) and others that it is increased (Murphy et al. 2011; Boly et al. 2012b; Lee et al. 2017b). Furthermore, selective effects of anesthesia have been reported on both feedback (Lee et al. 2013; Murphy et al. 2019) and feedforward (Sanders et al. 2018) connectivity. Decreased thalamo-cortical connectivity has been reported for both anesthesia and sleep (Alkire et al. 2000; Picchioni et al. 2014), but at least for anesthesia this change is unlikely to be causal for LOC (Hudetz 2012).

Distinct effects of anesthesia and sleep on network properties have also been reported. Increased modularity of resting state networks during non-rapid eye movement (REM) sleep was reported to be accompanied by greater connectivity overall (Boly et al. 2012b), suggesting differential effects on within- versus between-network connectivity. By contrast, during propofol anesthesia both between- and within-network connectivity was observed to decrease (Boveroux et al. 2010; Golkowski et al. 2019). Investigations that operationalized changes in brain integration (Schrouff et al. 2011; Boly et al. 2012b) and differentiation (Massimini et al. 2005; Ferrarelli et al. 2010; Casali et al. 2013; Sarasso et al. 2015) have yielded more consistent results. However, a direct comparison of these effects during anesthesia and sleep would provide more direct evidence for their roles in LOC and ROC.

Recently, we reported consistent changes in cortical functional connectivity during anesthesia and sleep (Banks et al. 2020). Stages of higher probability of consciousness, including wake and N1 and REM sleep (when dreaming is prominent), exhibited connectivity profiles that were similar to each other but distinct from stages of reduced probability of consciousness such as propofol unresponsiveness and non-REM sleep (Banks et al. 2020). These findings were consistent with a network transition boundary for consciousness common to anesthesia and sleep, but did not yield a unifying framework for understanding network reorganization and relating these changes to theoretical constructs (Dehaene and Changeux 2011; Mashour 2014; Tononi et al. 2016).

Here, we explore the organization of cortical networks using intracranial electroencephalogrqphic (EEG) recordings from neurosurgical patients. We apply diffusion map embedding (DME) (Coifman et al. 2005; Coifman and Hirn 2014) to functional connectivity measured between recording sites. DME has been used previously to demonstrate an intrinsic or "functional" geometry of brain networks based on time series data (Langs et al. 2010; Margulies et al. 2016). Since these initial applications in the field of neuroscience, DME has been used with increasing frequency to explore the relationship between structure and function in the brain (Liu et al. 2022; Meng et al. 2022; Parkes et al. 2022; Chiou et al. 2023; Katsumi et al. 2023; Pines et al. 2023), and changes in brain networks underlying altered states of consciousness (Huang et al. 2021a; Huang et al. 2023; Timmermann et al. 2023) and brain and psychiatric disorders (Hong et al. 2019; Oldehinkel et al. 2023; Yang et al. 2023). DME maps the anatomical locations of recording sites into a Euclidean embedding space in which proximity reflects similarity in connectivity to the rest of the network. Implicit in this analytical framework is the assumption that two sites that are similarly connected to the rest of the brain are performing similar functions.

In this study, we identify differences in the organization of cortical networks between stages of sleep and anesthesia that may underlie LOC. As in our previous work, we distinguished stages corresponding to substantially reduced probability of consciousness (propofol unresponsiveness, non-REM sleep) from the waking state and from stages of higher probability of conscious experience (propofol sedation, light sleep, REM sleep). We show that states of reduced consciousness during both anesthesia and sleep can be characterized reliably by a single parameter, the effective dimensionality of the normalized connectivity matrix. We present an analytical framework that provides an intuitive, geometric understanding of changes in cortical networks associated with states of reduced consciousness and observed reductions in effective dimensionality. Globally, brain regions become more distinct (reduced *functional integration*), moving farther apart in functional embedding space. Locally, brain subregions become less distinguishable (reduced *differentiation*), moving closer to each other in the functional embedding space. This unifying framework has a practical utility in identifying cortical state transitions in clinical settings and broader implications for understanding the neural basis of consciousness.

Materials and methods
Data acquisition
Study participants

The study included 21 neurosurgical patients (eight female; age 18–54 years old, median age 34 years old) with medically refractory epilepsy and undergoing chronic invasive electrophysiological monitoring at the University of Iowa Hospital to identify seizure foci prior to resection surgery (Table 1). Patients were consented 11/2016–5/2021 and data collected 1/2017–6/2021. Research protocols aligned with recently aggregated best practices (Feinsinger et al. 2022) and were approved by the University of Iowa Institutional Review Board. Written informed consent was obtained from all participants. Research participation did not interfere with clinical care, and participants could rescind consent for research without interrupting their clinical management. All participants underwent neuropsychological assessment prior to electrode implantation, and none had cognitive deficits that would impact this study. As part of their clinical care, the dosages of the patients' anti-seizure medications (ASM) were gradually reduced during chronic monitoring when resting state data were collected. No a priori power analysis was performed to determine sample size; the obtained sample size is relatively large for studies of intracranial electrophysiology. In five participants, data from the same experiments were previously analyzed using a different approach (Banks et al. 2020).

Pre-implantation neuroimaging

All participants underwent whole-brain high-resolution T1-weighted structural magnetic resonance imaging (MRI) scans before electrode implantation. The scanner was a 3 T GE Discovery MR750W with a 32-channel head coil. The T1 scan (3D FSPGR BRAVO sequence) was obtained with the following parameters: Field of View (FOV) = 25.6 cm, flip angle = 12°, Repetition Time (TR) = 8.50 ms, Time to Echo (TE) = 3.29 ms, inversion time = 450 ms, voxel size = 1.0 × 1.0 × 0.8 mm.

Intracranial EEG recordings

Intracranial EEG (iEEG) recordings were obtained using either subdural and depth electrodes, or depth electrodes alone. The type and placement of electrodes were decided solely on the basis of clinical requirements, as determined by the team of epileptologists and neurosurgeons (Nourski and Howard 3rd. 2015). Electrode arrays were manufactured by Ad-Tech Medical (Racine, WI). Subdural arrays, implanted in 14 participants out of 21, consisted of platinum-iridium disks (2.3 mm diameter, 5–10 mm inter-electrode distance), embedded in a silicon membrane. Stereotactically implanted depth arrays included between 4 and 12 cylindrical contacts along the electrode shaft, with 5–10 mm

Table 1. Subject demographics and summary of anesthesia and sleep data.

| | | | Clinical background | | | Recording duration (min) | | | | | | | | | |
| | | | | | | Propofol | | | | Sleep | | | | | |
Subject	Age	Sex	MRI	PET	Seizure focus	W	S	U	Total	W	N1	N2	N3	REM	Total
R369	30	M	R basal ganglia deep venous anomaly	R mesial temporal hypometabolism	R medial temporal	-	-	-	-	98	5	10	0	0	113
L372	34	M	Normal	L mesial temporal hypometabolism	L temporal pole	6	1	7	14	126	16	178	0	47	367
R376	48	F	L and R frontal white matter small vessel ischemic disease	Normal	R medial temporal	6	6	6	18	148	12	285	42	47	534
R384	38	M	R mesial temporal sclerosis	R anterior and mesial temporal hypometabolism	R medial temporal	6	0	12	18	-	-	-	-	-	-
R394	24	M	R anterior and medial temporal post-surgical change	R temporal hypometabolism	R amygdala (medial temporal)	6	6	6	18	-	-	-	-	-	-
R399	22	F	Normal	R lateral and superior temporal hypometabolism	R temporal (uncertain medial & neocortical)	5	1	7	13	-	-	-	-	-	-
L400	59	F	L mesial temporal sclerosis, L dorsolateral prefrontal volume loss	L hemisphere diffuse hypometabolism except occipital lobe	L amygdala (medial temporal)	6	7	1	14	-	-	-	-	-	-
L403	56	F	Normal	R mesial temporal slight hypometabolism	L medial temporal	6	1	7	14	111	30	141	0	1	283
L405	19	M	Left frontal encephalomalacia	L frontal hypometabolism	L frontal (posterior lateral)	6	1	7	14	-	-	-	-	-	-
L409	31	F	L amygdala enlargement, L medial temporal choroidal fissure cyst	L mesial temporal hypometabolism	L medial temporal, L temporal pole	6	7	1	14	165	46	189	9	82	491
R413	22	M	R medial temporal subtle FLAIR signal change	R anterior and medial temporal hypometabolism	right medial temporal	6	6	9	21	-	-	-	-	-	-
R418	25	F	R posterior lateral ventral cortex developmental malformation	R temporal hypometabolism	R temporal (medial & lateral posterior cortex)	6	12	6	24	132	34	253	34	150	603
L423	51	M	Normal	Normal	L medial temporal	6	7	7	20	307	32	199	20	42	600
L439	37	M	Right parieto-occipital encephalomalacia, bilateral frontal R basal ganglia gliosis	Not done	R medial frontal (posterior dorsal)	-	-	-	-	199	32	75	65	0	371
L457	18	M	Normal	Normal	L medial temporal	-	-	-	-	282	10	180	70	77	619
L460	52	M	Normal	L medial temporal hypometabolism	L hippocampus (medial temporal)	-	-	-	-	70	43	243	41	30	427
L514	46	M	L insula atrophy	Normal	L insula (anterior)	6	0	6	12	74	67	338	10	39	528
R524	18	M	Normal	R anterior and medial temporal hypometabolism	R medial temporal, L medial temporal	-	-	-	-	63	7	315	28	65	478
R532	42	F	Normal	R medial temporal hypometabolism	R ventral frontal (posterior)	-	-	-	-	341	21	186	5	83	636
R567	33	M	Normal	Not done	R insula	-	-	-	-	315	105	251	8	0	679
L585	39	F	L anterior temporal gray-white matter differentiation blurring	L anterior temporal hypometabolism	L medial temporal	10	0	6	16	223	34	191	41	162	651

MRI = magnetic resonance imaging; PET = positron emission tomography; W = wake; S = sedated; U = unresponsive; REM = rapid eye movement; R = right; L = left.

inter-electrode distance. A subgaleal electrode, placed over the cranial vertex near midline, was used as a reference in all participants. For sleep recordings, data were recorded using a Neuralynx Atlas System (Neuralynx Inc., Bozeman, MT), amplified, filtered (0.1–500 Hz bandpass, 5 dB/octave rolloff), and digitized at a sampling rate of 2,000 Hz. For anesthesia recordings, data were acquired using a TDT RZ2 real-time processor (Tucker-Davis Technologies, Alachua, FL) in participants R369 through L460 and by a Neuralynx Atlas System in participants L514 and L585. Recorded data were amplified, filtered (0.7–800 Hz bandpass, 12 dB/octave rolloff for TDT-recorded data; 0.1–500 Hz bandpass, 5 dB/octave rolloff for Neuralynx-recorded data), and digitized at a sampling rate of 2034.5 Hz (TDT) or 2000 Hz (Neuralynx).

Sleep recordings

Resting-state iEEG, EEG, and video data were recorded during overnight sleep ($n = 15$ participants) 7.5 +/− 1.1 days [range 6–9] after iEEG electrode implantation surgery. All participants (i) in whom placement of overnight scalp EEG leads did not interfere with clinical monitoring, and (ii) that had at least 10 data acquisition channels available to accommodate scalp EEG, electromyogram (EMG), and electrooculogram (EOG) leads in addition to iEEG are included in this cohort. Per clinical limitations and for patient's comfort, overnight sleep data were recorded with scalp EEG on one, and occasionally ($n = 2$ participants) two, nights during the monitoring period. If two nights of data were collected, one was randomly chosen to be analyzed. Data were collected in the dedicated, electrically shielded suite in The University of Iowa Clinical Research Unit while the participants lay in the hospital bed.

Stages of sleep [wake (WS), N1, N2, N3, REM] were defined manually using facial EMG and scalp EEG data based on standard clinical criteria (Berry et al. 2017). Sleep staging was performed independently by two individuals who participate in the inter-scorer reliability program of the American Academy of Sleep Medicine: a licensed polysomnography technologist, certified by the Board of Registered Polysomnography Technologists, and a physician certified in Sleep Medicine by the Accreditation Council for Graduate Medical Education. The final staging report was agreed upon by the two scorers after a collaborative review. Scalp and facial electrodes were placed by an accredited technician, and data were recorded by a clinical acquisition system (Nihon Kohden EEG-2100) in parallel with research data acquisition. Facial electrodes were placed following guidelines of the American Academy of Sleep Medicine (Berry et al. 2017) at the left and right mentalis for EMG, and adjacent to left and right outer canthi for EOG. EEG was obtained from electrodes placed following the international 10–20 system at A1, A2, F3, F4, O1, and O2 in all participants, with the following additional electrodes: C3 and C4 in all participants but R376; Cz and Fz in L409, L423, and L585; F7 in L585; F8 in L423 and L585. One participant (L403) experienced multiple seizures in the second half of the night; those data were excluded from analysis. The durations of recordings for each sleep stage in each participant are provided in Table 1.

Anesthesia recordings

Anesthesia data were collected during induction of propofol anesthesia ($N = 14$ participants) prior to electrode removal surgery, typically 2 weeks after implantation. All participants undergoing propofol induction are included in this cohort. Data were collected during an awake baseline period and during either an infusion of increasing doses of propofol ($n = 12$; 50–150 μg/kg/min) or a propofol bolus followed by constant infusion

($n = 2$; Supplemental Fig. 1). Participants were observed to have eyes closed during nearly all resting state recordings. Data were recorded in 3–4 blocks (duration 3–6 min each), interleaved with auditory stimulus paradigms related to other studies (e.g. Nourski et al. 2018; Nourski et al. 2021).

Awareness was assessed using the Observer's Assessment of Alertness/Sedation (OAA/S) scale (Chernik et al. 1990) just before and just after collection of each resting state data block. Data segments were assigned labels corresponding to one of three anesthesia stages: wake (WA; i.e. pre-drug), sedated but responsive to command (S; OAA/S ≥ 3), and unresponsive (U; OAA/S ≤ 2) (Nourski et al. 2018) (Supplemental Fig. 1). Bispectral index (Gan et al. 1997) was measured but was not used in the analyses presented in this study.

In six participants, OAA/S values crossed the boundary between S and U during the resting state block (e.g. resting state block #1 in participant L372; see Supplemental Fig. 1). In these cases, only the first and last 60-s segments of the block were analyzed; data from the first segment were labeled S, and data from the second segment were labeled U. Data in the intervening segment were not used in the analysis. The durations of recordings used in the analyses for each stage and each participant during the anesthesia experiment are provided in Table 1.

Data analysis

Anatomical reconstruction and region of interest parcellation

Localization of recording sites and their assignment to region of interest (ROIs) relied on post-implantation T1-weighted anatomical MRI and post-implantation computed tomography, as described previously (Banks et al. 2020). All images were initially aligned with pre-operative T1 scans using linear coregistration implemented in FSL (FLIRT) (Jenkinson et al. 2002). Electrodes were identified in the post-implantation MRI as magnetic susceptibility artifacts and in the computerized tomography (CT) scan as metallic hyperdensities. Electrode locations were further refined within the space of the pre-operative MRI using three-dimensional non-linear thin-plate spline warping (Rohr et al. 2001), which corrected for post-operative brain shift and distortion. The warping was constrained with 50–100 control points, manually selected throughout the brain, which were visually aligned to landmarks in the pre- and post-implantation MRI.

To sort recording sites for presentation of diffusion matrices and for assessment of centroid distances and clustering, recording sites were assigned to one of 58 ROIs (Fig. 1, Supplemental Table 1). These ROIs were categorized into nine functional regions based on analysis of resting state data from a different cohort of participants (Banks et al. 2022). (A small number of sites in ROIs that did not appear in that cohort were grouped with regions based on anatomical and functional criteria.) In the current study, recording sites were assigned to ROIs based on anatomical reconstructions of electrode locations in each participant. For subdural arrays, ROI assignment was informed by automated parcellation of cortical gyri (Destrieux et al. 2010; Destrieux et al. 2017) as implemented in the FreeSurfer software package. For depth arrays, it was informed by MRI sections along sagittal, coronal, and axial planes. Subcortical recording sites identified as seizure foci or characterized by excessive noise, and depth electrode contacts localized to the white matter or outside brain, were excluded from analyses and are not listed in Supplemental Table 1.
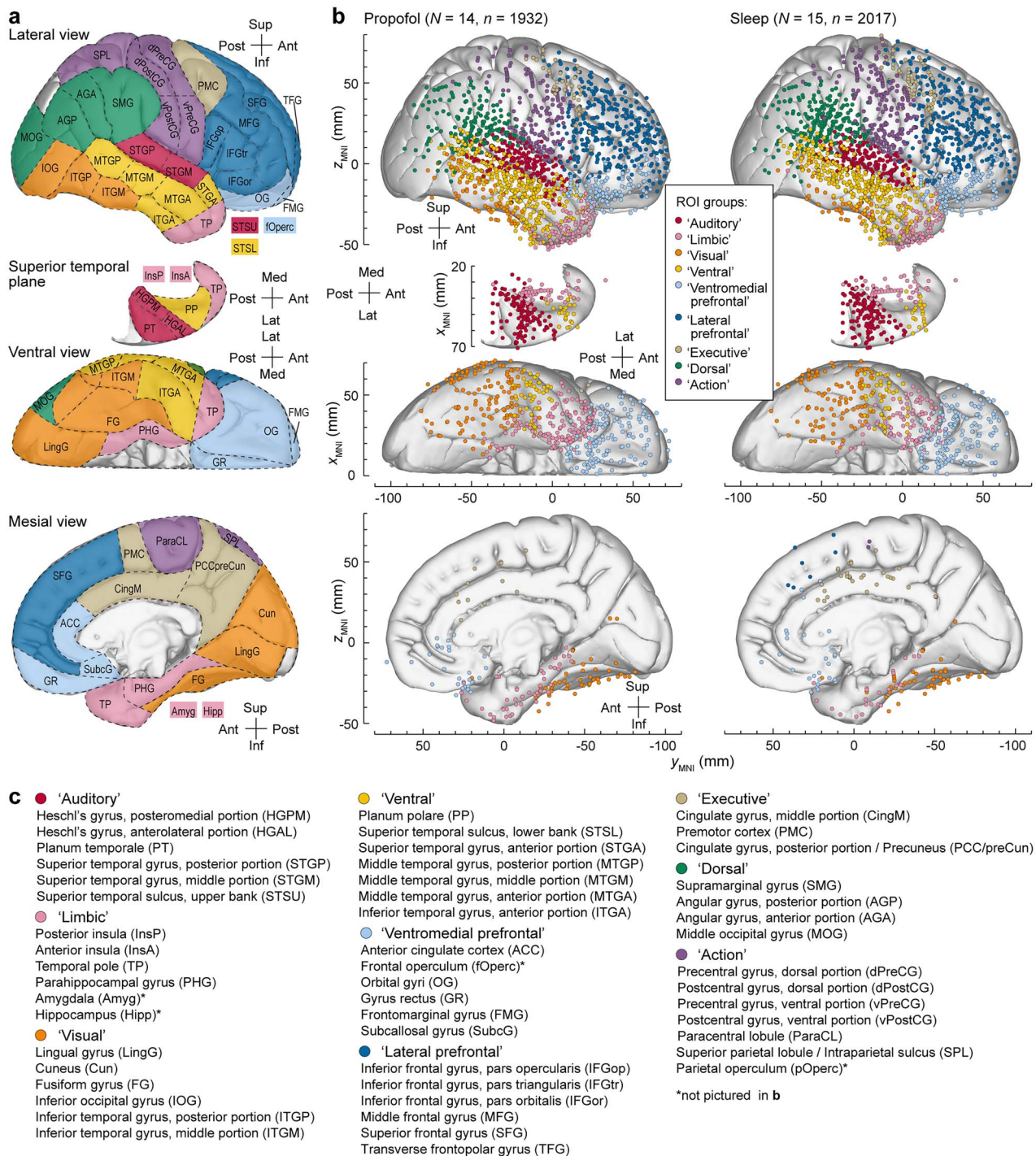
Fig. 1. ROI parcellation and electrode coverage. (a) ROI parcellation scheme used in the present study. (b) Electrode coverage in all subjects that contributed to the propofol and sleep data sets (left and right column, respectively). Locations of recording sites, color-coded according to functional region, are plotted in MNI coordinate space and projected onto the right hemisphere of the MNI152 average template brain for spatial reference. (Note that assignment of recording sites to ROIs was made based on anatomical reconstructions specific to each participant rather than based on the projection onto the template brain, thus accounting for the individual variability in cortical anatomy; see Materials and methods for details.) Left hemisphere MNI x-axis coordinates (x_{MNI}) were multiplied by −1 to map them onto the right-hemisphere common space. Projection is shown on the lateral, top-down (STP), ventral and mesial views, aligned with respect to the y_{MNI} coordinate (top to bottom rows). Recording sites over orbital, frontomarginal, inferior temporal gyrus, and temporal pole are shown in both the lateral and the ventral view. Sites in fusiform, lingual, parahippocampal gyrus, and gyrus rectus are shown in both the ventral and medial view. Sites in the amygdala, frontal operculum, hippocampus, and parietal operculum are not shown. (c) ROI groups, ROIs, and abbreviations used in the present study.

Preprocessing of iEEG data

Analysis of iEEG data was performed using custom software written in MATLAB (MathWorks, Natick, MA, USA). Several automated steps are taken to exclude recording channels and time intervals contaminated by noise. First, channels were excluded if average power in any frequency band (broadband, delta (1–4 Hz), theta (4–8 Hz), alpha (8–14 Hz), beta (14–30 Hz), gamma (30–50 Hz), or high gamma (70–110 Hz); see below) exceeded 3.5 standard deviations

of the average power across all channels for that participant. Next, transient artifacts were detected by identifying voltage deflections exceeding 10 standard deviations on a given channel. A time window was identified extending before and after the detected artifact until the voltage returned to the zero-mean baseline plus an additional 100 ms buffer before and after. High-frequency artifacts were also removed by masking segments of data with high gamma power exceeding five standard deviations of the mean across all segments. Only time bins free of these artifact masks were considered in subsequent analyses. Artifact rejection was applied across all channels simultaneously so that all connectivity measures were derived from the same time windows. Occasionally, particular channels survived the initial average power criteria yet had frequent artifacts that led to loss of data across all the other channels. There is a tradeoff in rejecting artifacts (losing time across all channels) and rejecting channels (losing all data for that channel). If artifacts occur on many channels, there is little benefit to excluding any one channel. However, if frequent artifacts occur on one or simultaneously on up to a few channels, omitting these can save more data from other channels than those channels contribute at all other times. We chose to optimize the total data retained, channels × time windows, and omitted some channels when necessary. The number of channels and percent of recording time retained for each participant is reported in Supplemental Table 2.

On occasion, broadband noise from in-room clinical equipment and muscle artifacts appeared in the data as shared signals across channels. This noise could be detected via analysis of frequencies higher than those of interest here. To remove these signals, data from retained channels were high-pass filtered above 200 Hz, and a spatial filter was derived from the singular value decomposition of the data omitting the first singular vector. This spatial filter was then applied to the broadband signal to remove the common signal. This procedure was implemented as follows. Note that here and throughout, upper case bold letters refer to matrices, and lower case bold letters refer to vectors.

For the matrix $\mathbf{Y}_{HP}$ of N samples of high-pass filtered data from M recording sites, and the covariance matrix $C_{M \times M} = \mathbf{S} \left(\mathbf{Y}_{HP}^T \mathbf{Y}_{HP} \right) \mathbf{S}$, where

$$\mathbf{S} = \begin{bmatrix} 1/\sigma_1 & 0 & \cdots \\ 0 & \ddots & \vdots \\ \vdots & 0 & 1/\sigma_M \end{bmatrix},$$

and σ_i = standard deviation of high-passed filtered signal from the ith recording site, $\mathbf{Y}_{HP,i}$, the singular value decomposition of $C_{M \times M}$ is obtained as

$$C_{M \times M} = [\boldsymbol{u}_1, \boldsymbol{u}_2, \ldots, \boldsymbol{u}_M] \begin{bmatrix} \lambda_1 & 0 & \cdots \\ 0 & \ddots & 0 \\ \vdots & 0 & \lambda_M \end{bmatrix} [\boldsymbol{u}_1, \boldsymbol{u}_2, \ldots, \boldsymbol{u}_M]^T,$$

where $\boldsymbol{u}_i$ are eigenvectors, and λ_i are eigenvalues of $C_{M \times M}$. The spatial filter is defined as

$$\mathbf{W}_{SVD} = \mathbf{S} \left(I_{M \times M} - \boldsymbol{u}_1 \boldsymbol{u}_1^T \right) \mathbf{S}^{-1},$$

where $\mathbf{I}_{M \times M}$ is the identity matrix. The spatial filter is applied to the unfiltered data, $\mathbf{Y}$, as

$$\mathbf{Y}_{SVD} = \mathbf{Y} \mathbf{W}_{SVD}.$$

The purpose of the initial high-pass filtering in computing the spatial filter, $\mathbf{W}_{SVD}$, is to minimize the influence of long-range physiological correlations, which tend to be associated with low frequency oscillations (Leski et al. 2013), on $\mathbf{C}_{M \times M}$, while preserving zero-lag correlations arising from reference contamination and other potential artifactual sources.

Connectivity analysis

For connectivity analysis, the orthogonalized gamma band (30–70 Hz) power envelope correlation (Hipp et al. 2012) was used. This measure avoids artifacts due to volume conduction by discounting connectivity near zero phase lag. We focused here on a specific functional connectivity measure (orthogonalized power envelope correlations) and a specific frequency band (gamma) because a parallel study demonstrated their utility for performing DME analysis (Banks et al. 2022). Gamma band connectivity is also strongly related to connectivity derived from functional MRI (Hacker et al. 2017), allowing comparisons to neuroimaging studies of anesthesia and sleep. We show that the main result of the paper regarding D_E is largely robust to choice of frequency band (Supplemental Fig. 5). Data were divided into 60-s segments and envelope correlations estimated for each pair of recording sites as in (Hipp et al. 2012), except time-frequency decomposition was performed using the demodulated band transform (Kovach and Gander 2016), rather than wavelets. Briefly, the procedure was as follows. Envelope correlations were calculated between each pair of recorded voltages x(t) and y(t). The time-frequency representations X(t,f) and Y(t,f) were calculated using the demodulated band transform (Kovach and Gander 2016). For each pair of complex signals $X(t,f)$ and $Y(t,f)$, one was orthogonalized to the other by taking the magnitude of the imaginary component of the product of one signal with the normalized complex conjugate of the other:

$$Y_{orth} = \left| \text{Im} \left\{ Y \times X^* / |X| \right\} \right|$$

Gamma power at each time bin was then calculated as the average (across frequencies) log of the squared amplitude. Both power signals were bandpass filtered (0.2–1 Hz), and the Pearson correlation calculated between signals. The process was repeated by orthogonalizing in the other direction and the overall envelope correlation for a pair of recording sites was the average of the two Pearson correlations.

Prior to DME, connectivity matrices were thresholded by saving at least the top third (rounded up) connections for every row, as well as their corresponding columns (to preserve symmetry). We also included any connections making up the minimum spanning tree of the graph represented by the element wise reciprocal of the connectivity matrix to ensure the graph is connected.

To confirm that the results presented were robust to the specific threshold chosen, two additional thresholds were tested: (i) a stricter procedure, as above except saving only the top 10%, or (ii) a more permissive procedure, only thresholding out negative correlations.

Diffusion map embedding

See Banks et al. (2022) for details about DME. In brief, cosine similarity was applied to the functional connectivity matrix to yield the similarity matrix $\mathbf{K} = [k(i,j)]$, which was normalized by degree to yield a diffusion matrix $\mathbf{P} = \mathbf{D}^{-1} \mathbf{K}$. $\mathbf{D}$ is the degree matrix, i.e. the diagonal elements of $\mathbf{D} = \sum_{j=1}^{N} k(i,j)$, where N is the number of recording sites, and the off-diagonal elements of $\mathbf{D}$ are zero. If the recording sites are conceptualized as nodes on a graph with edges defined by $\mathbf{K}$, then $\mathbf{P}$ can be understood as the transition

probability matrix for a "random walk" or a "diffusion" on the graph (see Coifman et al. 2005; Coifman and Hirn 2014). DME consists of mapping the recording sites into an embedding space using the eigen decomposition of **P**,

$$\Psi^{(t)}(x_i) = \left[\lambda_1{}^t \psi_1(x_i), \lambda_2{}^t \psi_2(x_i), \dots, \lambda_M{}^t \psi_M(x_i) \right],$$

Where $M < N$ is the number of retained dimensions (see below). λ_i and ψ_j are the eigenvalues and eigenvectors of **P**, respectively. Because of the properties of **P**, $\lambda_1 = 1$ and its corresponding eigenvector is approximately constant and thus does not contribute to the structure of the data in embedding space. Thus, it is standard practice to omit that first dimension (Coifman and Hirn 2014) and that was done here. The parameter t is the number of time steps in that random walk; here, we fix $t = 1$. DME can be implemented alternatively based on a symmetric version of diffusion matrix $\mathbf{P_{symm}} = \mathbf{D}^{-0.5}\mathbf{K}\mathbf{D}^{-0.5}$. Basing DME on $\mathbf{P_{symm}}$ has the advantage that the eigenvectors of $\mathbf{P_{symm}}$ form an orthogonal basis set (unlike the eigenvectors of **P**), providing some additional convenience mathematically that is beyond the scope of this paper (Coifman and Hirn 2014). Of note, the eigenvalues of **P** and $\mathbf{P_{symm}}$ are identical.

Effective dimensionality

We used effective dimensionality (D_E) (Del Giudice 2021), a graph theoretic measure of network complexity, to characterize the shape of the spectrum of $\mathbf{P_{symm}}$, or equivalently the complexity of its community structure. D_E was calculated from the eigenvalue spectrum $|\lambda_i|$ of $\mathbf{P_{symm}}$ and normalized to the total number of dimensions (N; equal to the number of recording sites) as

$$D_E = \left(\sum_{i=2}^{N} \lambda_i \right)^2 / \sum_{i=2}^{N} \lambda_i^2 / (N - 1).$$

To maintain consistency with DME above, the first dimension, for which $\lambda_1 = 1$, is omitted. D_E gives information about how data is distributed in N dimensions. $D_E = 1$ for a random graph, as the data are distributed equally in every dimension and the spectrum is flat. A graph with structure, e.g. nodes that connect to each other more than the rest of the graph, has a peaked spectrum and $D_E < 1$.

Clustering of functional regions in embedding space

Two measures were used to quantify the arrangement of nodes in embedding space according to brain region. First, the distance between regions in embedding space was measured by the pairwise (by region) Euclidean distance between centroids (mean position across nodes within each region). Second, the Calinski-Harabasz index of cluster quality [the ratio of between-cluster variance to within-cluster variance; (Caliński and Harabasz 1974)] was used to quantify the extent to which nodes segregated in embedding space according to these pre-identified functional regions.

Local distance

To quantify the tendency of nodes to be functionally distinct from other nodes (or, conversely, to aggregate in embedding space and be less differentiated) without needing to rely on assignments of nodes to pre-defined ROIs or regional groupings, we defined a measure called "local distance" as the mean Euclidean distance in embedding space from a given node to each of the 5% closest other nodes, divided by the median distance to all pairs of nodes.

Dimensionality reduction via low rank approximations to P_{symm}

When calculating distances or evaluating clustering in embedding space, we used a low rank approximation, discarding dimensions associated with small eigenvalues that are likely dominated by noise. We used an algorithm to identify the inflection point k_{infl} beyond which eigenvalues are small and decrease gradually (Satopaa et al. 2011), and the number of dimensions retained set equal to $k_{infl} - 1$. The algorithm calculates points of maximum curvature in smoothed data. Since each data segment can potentially have a different inflection point and to avoid using a different number of dimensions for each data segment, we used the 90th percentile across data segments for all segments for each participant in that experiment. For propofol, the median # of dimensions kept was 14, range [6, 21]; for sleep, the median was 14, range [8, 21].

Spectral analysis

For each participant, power was calculated using the demodulated band transform (Kovach and Gander 2016) in delta (1–4 Hz) and gamma (30–50 Hz) bands for each recording site and then averaged (mean) across recording sites.

Statistical modeling

All measures (D_E, centroid distance, Calinski-Harabasz index, local distance) were computed for individual data segments, then averaged within each participant across all segments of the with the same stage label (WA, S, U, WS, N1, N2, N3, REM). The study design has minimal potential for bias on the effect of stage, as participants were not assigned or filtered into groups; instead, each participant provided data from stages associated with both high and low probability of consciousness. Linear mixed effects models were fit to these measures with behavioral state as a fixed effect and participant as a random effect; fit models were compared to a reduced model omitting the fixed effect for stage using a likelihood ratio test. Mixed effects models control for confounding by repeated measures in the same individuals and are suitable for factorial designs with missing data; no attempt to impute missing data was performed. No other predictor variables besides stage were included in the models. Pairwise planned contrasts were tested between WA-S, WA-U, and S-U for propofol experiments, and WS-N1, WS-N2, WS-N3, WS-REM, N1-N2, N2-N3, N2-REM, and N3-REM for sleep experiments; P-values were adjusted using a multivariate t-distribution that accounts for correlations among tested hypotheses. Statistical analyses were performed in R version 4.2.1 using the packages lme4 (Bates et al. 2015) and emmeans (Lenth 2019).

In the primary analysis, recordings from all brain areas were used to derive each measure from the diffusion matrix or embedding space. However, it is possible that specific brain areas are responsible for the observed differences between stages. Therefore, we conducted sensitivity analyses by excluding brain regions as if those regions were not recorded. Statistical models were the same as described above.

Data and code availability

Data reported in this paper will be shared by the lead contact upon request. All original code and the data that appears in the figures have been deposited at Zenodo https://doi.org/10.5281/zenodo.7897507 and is publicly available as of the date of publication.
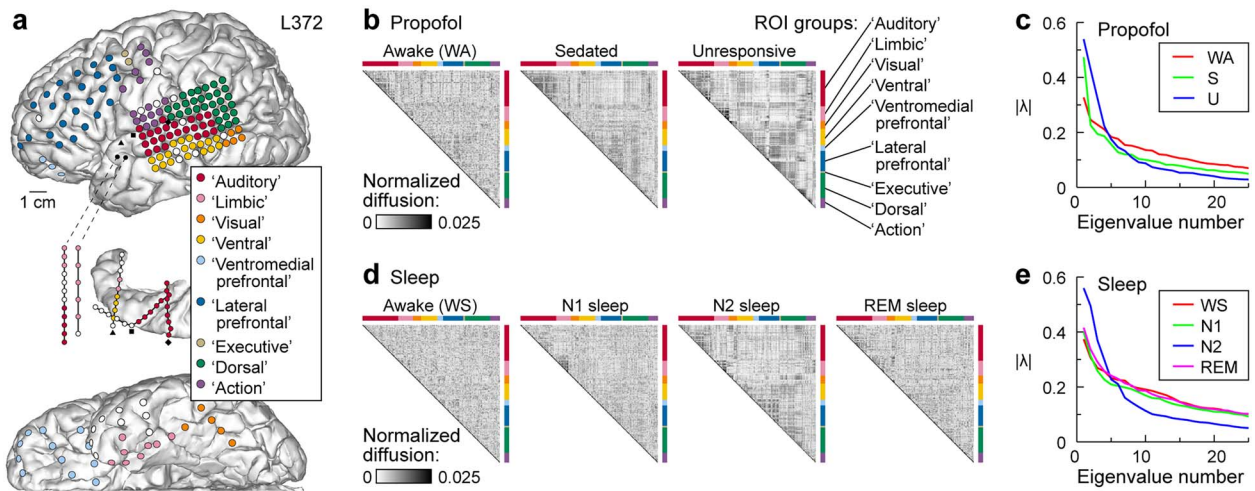
Fig. 2. Network organization varies during anesthesia and sleep. Data from a representative participant (L372). (a) Electrode coverage in this participant. Recording sites are color-coded according to the ROI group. White symbols denote sites excluded from the analysis due to excessive noise, artifacts, location within seizure focus, in white matter, or outside the brain. Black symbols denote depth electrode insertion points. (b) Diffusion matrices $\mathbf{P_{symm}}$ during propofol anesthesia for the participant in (a). Each matrix is from 1 min of data. (c) Spectra of $\mathbf{P_{symm}}$ calculated from the example matrices in (b). For these examples, $D_E(WA) = 0.30$, $D_E(S) = 0.20$, $D_E(U) = 0.10$. (d) Diffusion matrices $\mathbf{P_{symm}}$ during sleep for the participant in (a). Each matrix is from 1 min of data. (e) Spectra of $\mathbf{P_{symm}}$ calculated from the matrices in (d). For these examples, $D_E(WS) = 0.31$, $D_E(N1) = 0.30$, $D_E(N2) = 0.14$, $D_E(REM) = 0.32$. For panels (b)–(e), data recorded during anesthesia and sleep experiments were divided into segments of length 60 s, and the diffusion matrix and spectrum computed for each segment. Matrices and spectra shown are from the segments with effective dimensionality closest to the median value for each stage of anesthesia and sleep in this participant.

Results

Summary of experiments and recordings

Resting state iEEG recordings were obtained in neurosurgical patients undergoing intracranial monitoring for the purpose of identifying seizure foci. Demographic information is summarized in Table 1. Summaries of the brain parcellation scheme and of electrode coverage across all participants are shown in Fig. 1 and Supplemental Table 1, respectively. Typical electrode coverage is shown for one participant in Fig. 2a**.** Each recording site was assigned to a ROI, color-coded according to a functional parcellation scheme illustrated in Fig. 1a. This scheme was derived from analysis of resting state iEEG data from a complementary dataset obtained during daytime wake (Banks et al. 2022). To investigate changes in cortical network organization during transitions in arousal and awareness, data were recorded during induction of propofol anesthesia just prior to removal of electrodes (N = 14 participants; see Table 1 and Supplemental Fig. 1), and during overnight sleep (N = 15 participants; see Table 1 and Supplemental Fig. 2). As in our previous work, we identified stages of anesthesia (WA: pre-drug wake; S: sedated but responsive; U: unresponsive) using the OAA/S, a standard clinical assessment tool (Chernik et al. 1990; Banks et al. 2020). Sleep stages were identified using standard polysomnography (WS: wake; N1: light sleep; N2, N3: non-REM; REM). Three anesthesia participants had no data segments labeled "S," three sleep participants had no data segments labeled "N3," and three sleep participants had no data segments labeled "REM"; all other stages were present in all participants.

Altered cortical network organization during anesthesia and sleep

Functional connectivity was calculated as orthogonalized gamma band power envelope correlations (Hipp et al. 2012; Banks et al. 2022), yielding for each 1 min data segment an electrode × electrode connectivity matrix. The first steps of DME analysis are to create a similarity matrix by applying cosine similarity to the

functional connectivity matrix, then to normalize, threshold, and make symmetric the similarity matrix to yield a diffusion matrix $\mathbf{P_{symm}}$. $\mathbf{P_{symm}}$ describes the diffusion of an input signal applied to nodes (i.e. recording sites) on the graph (Coifman and Hirn 2014). When $\mathbf{P_{symm}}$ is sorted by brain region (indicated by colored bars in Fig. 2b), increasing community structure becomes evident in states of reduced consciousness under propofol anesthesia (sedated/S, unresponsive/U). The degree of community structure can be quantified by examining the eigenvalue spectrum of $\mathbf{P_{symm}}$ (Fig. 2c). Random graphs, i.e. those with maximal entropy, have spectra that are approximately flat. Graphs with strong community structure have spectra that are more peaked. The underlying entropy of the graph, and hence the shape of the spectrum, can be quantified using the effective dimensionality $D_E \in (0, 1)$, a function of the eigenvalue spectrum and a graph theoretic measure of complexity (see Materials and methods). Importantly, the eigenvalue spectrum and calculation of D_E do not require nodes to be ordered or labeled. Like anesthesia, non-REM sleep was associated with a more structured $\mathbf{P_{symm}}$ and more peaked spectrum (Fig. 2d and e).

The time series of D_E computed for each 60-s data segment recorded during an experiment reveals striking changes in network structure during both anesthesia and sleep experiments, with transitions into S and U during anesthesia and into N2 during sleep accompanied by sharp decreases in D_E (Fig. 3a). Notably, D_E was consistently higher during stages associated with higher probability of consciousness (WA, S, WS, N1, REM). Two additional examples from participants recorded during both propofol anesthesia and during sleep are shown in Supplemental Fig. 3.

Data were summarized across participants by first averaging D_E within participant across all segments associated with each stage of anesthesia and sleep. D_E varied significantly by stage for both propofol anesthesia and sleep (likelihood ratio test for omitting stage: propofol $\chi^2(2) = 42.0$, $P < 0.0001$; sleep $\chi^2(4) = 79.3$, $P < 0.0001$) (Fig. 3b). For propofol anesthesia, mean D_E decreased progressively from WA to S to U (Table 2). During sleep, D_E for N1 and REM were not significantly different from WS,
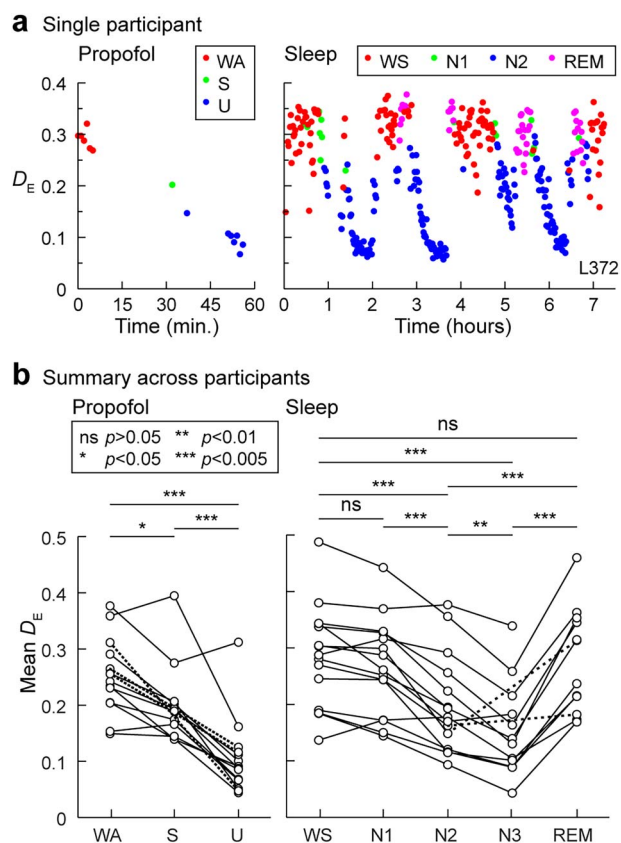
a Single participant

b Summary across participants

Fig. 3. Changes in D_E in states of reduced consciousness. (a) Time series of D_E from an example participant. Changes during anesthesia and sleep are shown in left and right panel, respectively. Each data point represents 1 min of data. Time is depicted relative to the start of recording. Same participant (L372) as in Fig. 2. (b) Summary of changes in D_E in states of reduced consciousness across all participants. Changes during propofol anesthesia and sleep are shown in left and right panel, respectively. Symbols are mean within a participant, connected by lines for data points from the same participant. Dashed lines are used to connect points when data in the intervening stage (S; N3) is not available for that participant. P-values are from paired post-hoc comparisons, adjusted using multivariate t-distribution.

but D_E decreased in N2 and decreased further in N3. These results were robust to the choice of threshold in calculating $\mathbf{P_{symm}}$ (Supplemental Fig. 4). Results were also robust to the choice of frequency band, with similar results obtained for alpha, beta, and high gamma band power envelope correlations (Supplemental Fig. 5). By contrast, spectral power alone did not reliably distinguish between stages of anesthesia and sleep (Supplemental Fig. 6).

Changes in cortical network organization are not regionally specific

It is plausible that observed changes in D_E between network states could be dominated by changes in a subset of recording sites in specific brain regions. We performed sensitivity analyses by repeating the analysis of Fig. 3b after excluding recording sites from groups of cortical functional regions (Supplemental Fig. 7; groups of regions were: Auditory, Limbic, Visual + Ventral, Ventromedial Prefrontal + Lateral Prefrontal + Executive, and Dorsal + Action). The significant decrease in D_E during states of reduced consciousness was observed in all cases, regardless of which regions were omitted. These results indicate that the

changes in network structure associated with transitions into states of reduced consciousness could not be explained by connectivity changes of any single brain region. Thus, anesthesia and sleep are associated with global reorganization of cortical networks.

Changes in effective dimensionality reflect decreased differentiation and functional integration

We've shown that D_E indexes entry and exit from states of reduced consciousness based on only the spectrum (eigenvalues) of $\mathbf{P_{symm}}$. The observed changes in D_E indicate a reorganization of brain networks; however, because there is no unique mapping between a spectrum and a network, changes in spectra do not identify the specific features of this reorganization. To gain insight into these features, we can apply the next steps in DME analysis and consider data in the embedding space defined by the spectral decomposition of $\mathbf{P_{symm}}$.

A simple toy model is useful in this regard (Fig. 4a). We simulated a modular network consisting of five regions, with nine nodes in each region. Two types of connectivity were present in the model: (i) uniform random connectivity linking nodes regardless of region, and (ii) stronger within-region connectivity imposed on this nonspecific random connectivity. The strength of within-region connectivity was varied from weak (Fig. 4a, left column) to strong (Fig. 4a, right column), corresponding to an increasingly modular organization of the network. This increase in modular organization (Fig. 4a, top row) was associated with more peaked eigenvalue spectra (insets in Fig. 4a) and decreased D_E. DME conveys the functional geometry of these changes in community structure by mapping the data into a lower dimensional embedding space using the eigenfunctions and eigenvalues of $\mathbf{P_{symm}}$ (Fig. 4a, bottom row). Nodes that are connected similarly to the rest of the network are mapped to nearby locations in the embedding space, indicating their functional similarity. A more modular network organization results in more tightly clustered nodes within each region; the neural responses of this more modular network would exhibit reduced differentiation. This is easily illustrated by considering the extreme case (right), in which the nodes within each region are so tightly coupled as to render them nearly equivalent, essentially transforming the original 45-node network into a 5-node network with a vastly reduced repertoire of possible network states. In addition, regions become more distinct and more distant from each other as modularity increases, corresponding to a decrease in functional integration across the whole network.

We observed similar changes in embeddings of functional connectivity data derived from intracranial recordings (Fig. 4b). Data recorded during states of reduced consciousness during propofol anesthesia (e.g. U; Fig. 4b, top row) or sleep (e.g. N2 or N3; Fig. 4b, bottom row) were "clumpier" in embedding space and regional clusters of nodes moved farther apart from each other, suggesting an increase in modularity.

We quantified these effects both with and without a priori assignments of electrodes to labeled clusters. Using labels from the nine regions illustrated in Fig. 1c, we assessed changes in cluster organization within embeddings. We measured inter-cluster distances between cluster centroids and regional grouping of nodes using an index of cluster quality (Calinski-Harabasz index) calculated as the ratio of between-cluster to within-cluster dispersion. We also considered the position of nodes in embedding space relative to their neighboring nodes without a priori assignments to functional regions. The analysis is illustrated in

Table 2. Post-hoc pairwise comparisons.

Measure	Contrast	Estimate, 95% CI	df	t	P
Mean D_E, propofol	S–WA	−0.048 [−0.090, −0.0068]	23.9	−2.92	0.020
	U–WA	−0.15 [−0.19, −0.11]	23.4	−9.74	<0.0001
	S–U	0.099 [0.058, 0.14]	23.9	6.01	<0.0001
Mean D_E, sleep	N1–WS	−0.018 [−0.051, 0.016]	50.0	−1.47	0.55
	N2–WS	−0.086 [−0.12, −0.052]	50.0	−7.04	<0.0001
	N3–WS	−0.13 [−0.17, −0.10]	50.2	−10.3	<0.0001
	R–WS	0.0047 [−0.031, 0.041]	50.2	0.362	1.00
	N1–N2	0.068 [0.034, 0.10]	50.0	5.57	<0.0001
	N2–N3	0.049 [0.013, 0.086]	50.2	3.78	0.0032
	N2–R	−0.090 [−0.13, −0.054]	50.2	−6.91	<0.0001
	N3–R	−0.14 [−0.18, −0.10]	50.2	−10.1	<0.0001
Centroid distance, propofol	S–WA	0.075 [0.019, 0.13]	23.1	3.34	0.0077
	U–WA	0.18 [0.13, 0.23]	23.0	8.96	<0.0001
	S–U	−0.11 [−0.16, −0.052]	23.1	−4.83	0.0002
Centroid distance, sleep	N1–WS	0.016 [−0.027, 0.059]	50.0	1.02	0.82
	N2–WS	0.059 [0.016, 0.10]	50.0	3.81	0.0028
	N3–WS	0.12 [0.069, 0.16]	50.0	6.92	<0.0001
	R–WS	0.021 [−0.025, 0.067]	50.0	1.24	0.70
	N1–N2	−0.043 [−0.086, −0.00037]	50.0	−2.79	0.047
	N2–N3	−0.056 [−0.10, −0.010]	50.0	−3.38	0.0097
	N2–R	0.038 [−0.0077, 0.084]	50.0	2.30	0.14
	N3–R	0.095 [0.046, 0.14]	50.0	5.36	<0.0001
Cluster quality, propofol	S–WA	3.9 [−1.1, 8.9]	23.4	1.97	0.14
	U–WA	10.7 [6.1, 15.2]	22.4	5.84	<0.0001
	S–U	−6.8 [−11.7, −1.8]	23.4	−3.41	0.0064
Cluster quality, sleep	N1–WS	1.9 [−2.9, 6.6]	50.3	1.09	0.78
	N2–WS	5.7 [0.98, 10.5]	50.3	3.33	0.011
	N3–WS	8.1 [3.0, 13.2]	50.9	4.38	0.0005
	R–WS	1.7 [−3.4, 6.8]	50.9	0.941	0.86
	N1–N2	−3.8 [−8.6, 0.90]	50.3	−2.24	0.16
	N2–N3	−2.4 [−7.4, 2.7]	50.8	−1.28	0.67
	N2–R	4.0 [−1.1, 9.1]	50.9	2.16	0.19
	N3–R	6.3 [0.94, 11.7]	51.1	3.25	0.014
Local distance, propofol	S–WA	−0.064 [−0.11, −0.015]	23.2	−3.31	0.0084
	U–WA	−0.19 [−0.24, −0.15]	22.2	−10.8	<0.0001
	S–U	0.13 [0.080, 0.18]	23.2	6.68	<0.0001
Local distance, sleep	N1–WS	−0.019 [−0.050, 0.013]	49.9	−1.64	0.44
	N2–WS	−0.078 [−0.11, −0.046]	49.9	−6.82	<0.0001
	N3–WS	−0.13 [−0.17, −0.10]	50.1	−10.9	<0.0001
	R–WS	−0.0058 [−0.040, 0.028]	50.1	−0.473	0.99
	N1–N2	0.059 [0.028, 0.091]	49.9	5.18	<0.0001
	N2–N3	0.056 [0.022, 0.090]	50.1	4.54	0.0003
	N2–R	−0.072 [−0.11, −0.038]	50.1	−5.87	<0.0001
	N3–R	−0.13 [−0.16, −0.092]	50.1	−9.82	<0.0001

CI = confidence interval; df = degrees of freedom, adjusted by Satterthwaite method.

Fig. 5a. For each node, we calculated a normalized "local distance" as the average pairwise distance to the 5th-percentile closest nodes normalized to the median distance to all nodes. Much like cluster quality, this measure captures combined aspects of differentiation (distance among similar nodes) and integration (distance between dissimilar nodes), but without requiring label assignments.

Systematic changes in all three measures were observed across stages of anesthesia (Fig. 5b, example participant). In U, inter-cluster distances increased, cluster quality improved, and local distances decreased. These results were consistent across subjects (likelihood ratio test for omitting stage: inter-cluster distance $\chi^2(2) = 37.8$, $P < 0.0001$; cluster quality $\chi^2(2) = 22.8$, $P < 0.0001$; local distance $\chi^2(2) = 47.9$, $P < 0.0001$; see pairwise comparisons in Table 2). Accordingly, effective dimensionality was negatively correlated with inter-cluster distance and cluster quality, and positively correlated with local distance (Fig. 5c). Similar relationships with sleep stage were observed in an example participant (Fig. 5d) and across participants (likelihood ratio test for omitting stage: inter-cluster distance $\chi^2(4) = 42.7$, $P < 0.0001$; cluster quality $\chi^2(4) = 22.5$, $P = 0.00016$; local distance $\chi^2(4) = 81.6$, $P < 0.0001$; see pairwise comparisons in Table 2) and were correlated with effective dimensionality (Fig. 5e).

For both sleep and anesthesia, the strongest correlations were observed between local distance and effective dimensionality. Local distance captures the reorganization in embedding space, and effective dimensionality allows for tracking changes in anesthesia or sleep stage, both without relying on a priori assumptions about the data.
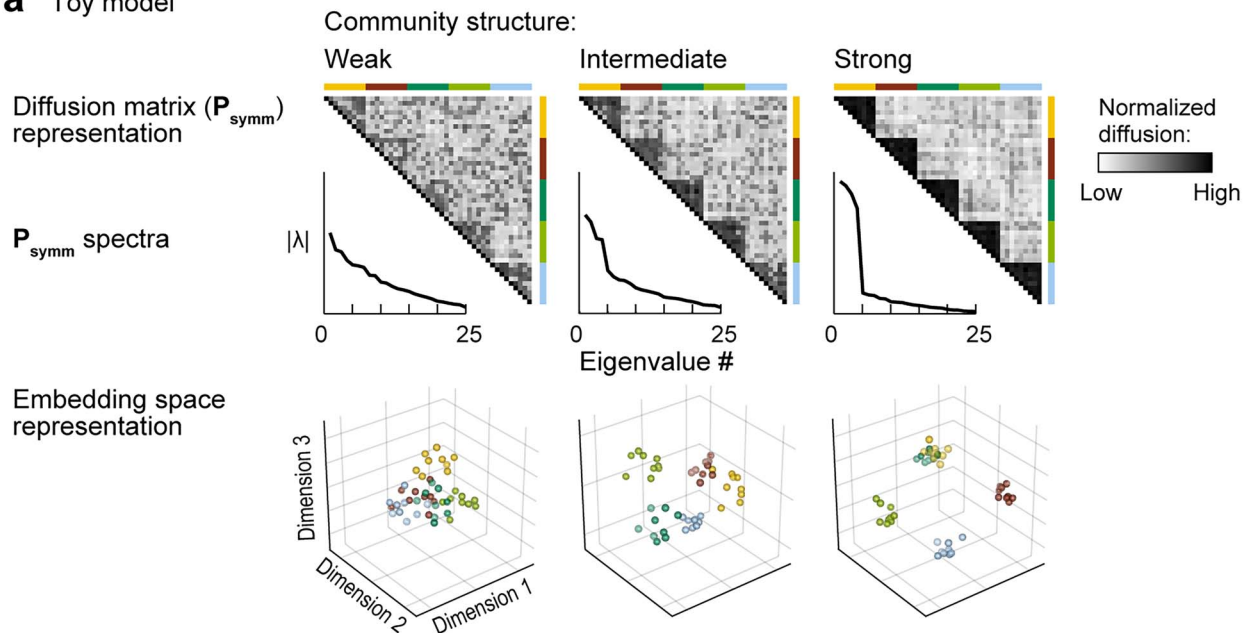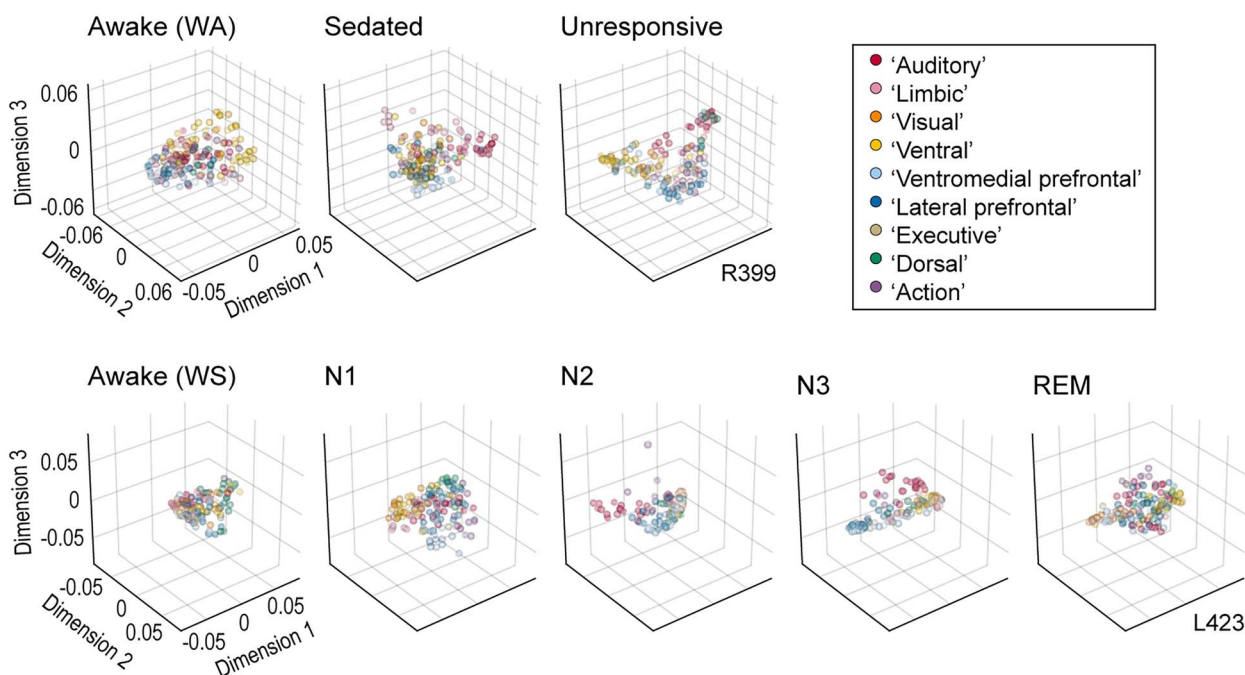
a Toy model

b Single participant examples

Fig. 4. Embedding space representation of community structure. (a) Toy example showing effects of stronger community structure on embeddings. Top row: Diffusion matrix ($\mathbf{P_{symm}}$) representation of weak, intermediate, and strong community structure (left, middle, and right panel, respectively). Insets depict $\mathbf{P_{symm}}$ spectra. D_E = 0.44, 0.35, 0.18, respectively. Bottom row: Embedding space representation of weak, intermediate, and strong community structure (left, middle, and right panel, respectively). Mean centroid distance = 0.35, 0.42, 0.50, respectively. (b) Changes in functional geometry during anesthesia and sleep in example participants. Top row: Arrangement of recorded data in embedding space (first three dimensions) during anesthesia in an example participant (R399). Each symbol represents an individual recording site. Colors indicate assignment to functional regions (legend). Bottom row: Arrangement of data in a second participant (L423) during sleep.

Discussion

Changes in effective dimensionality reflect changes in complexity, differentiation, and integration

We link changes in the organization of cortical networks with changes in consciousness during anesthesia and sleep using D_E.

D_E is related to spatial complexity, in that fewer dimensions are required to represent a less complicated network. Thus, the results presented here are consistent with decreased spatial complexity and smaller repertoire of distinct network configurations reported during LOC (Lee et al. 2010; Hudetz et al. 2014; Hutchison et al. 2014; Barttfeld et al. 2015; Lee et al. 2017a). Changes
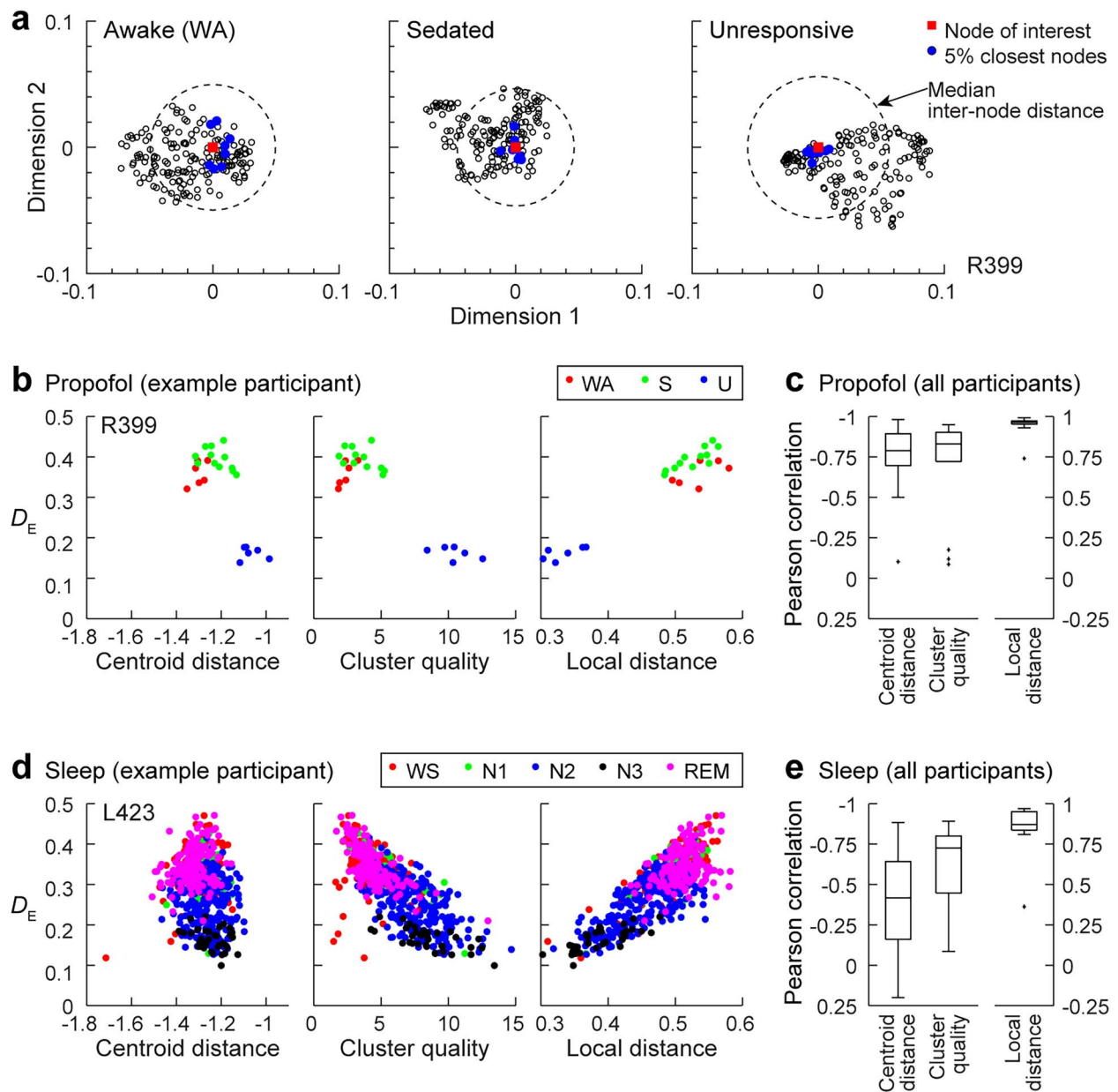
Fig. 5. Changes in embedding geometry are correlated with effective dimensionality. (a) Calculation for one node in one participant of normalized local distance, defined as the averaged distance between a node of interest and the 5% closest nodes, divided by the median distance to all nodes. Axes reflect distance along the first two dimensions from the reference node (*red square*). Shown are the closest 5% nodes (*filled blue circles*) and all other nodes (*open circles*). The closest nodes in the two dimensions shown are not necessarily the closest nodes in the higher-dimensional space. The radius of the dashed circle depicts the median Euclidean distance from the reference node to all nodes. Compared to awake, in unresponsive the closest nodes are even closer, while the median is larger. (b) Examples for a single participant (R399) of the relationships between D_E and centroid distance (*left*), cluster quality (*middle*), and local distance (*right*). Each point represents a 60-s segment of data. (c) Summary across participants of correlations between D_E and each embedding measure. Centroid distance and cluster quality are negatively correlated with D_E and presented on a reversed axis. The strongest association with D_E is with local distance. (d) Same as (b), but for sleep in L423. (e) Same as (c), but for sleep participants.

in simulated network modularity are reflected by changes in D_E (Fig. 4): when nodes are more tightly connected within each sub-network relative to connections to other sub-networks, D_E decreases. (We note that there is not a strict relationship between D_E and modularity, as it is theoretically possible to create a biologically unrealistic network with no modularity but low D_E.) In embedding space, this increase in modularity is reflected in increased cluster quality and a decrease in local distance (Fig. 5). Thus, the observation that D_E decreases during both anesthesia and sleep (Fig. 3) links the results presented here with previous fMRI results showing increased modularity during non-REM sleep

(Boly et al. 2012b). Reported decreases in within-network connectivity during anesthesia (Boveroux et al. 2010; Golkowski et al. 2019) are harder to reconcile with increased modularity, though this could reflect differences in the spatial scale of the analyses.

Proximity in embedding space corresponds to similarity in functional connectivity to the rest of the network. During states of reduced consciousness, recording sites become closer to their nearest neighbors (less distinguishable) in embedding space, suggesting reduced differentiation of their activity patterns. Consistent with these results, perturbational complexity, a measure of differentiation (Sarasso et al. 2021), shows consistent

decreases during anesthesia and sleep (Massimini et al. 2005; Ferrarelli et al. 2010; Casali et al. 2013; Sarasso et al. 2015). Similar results have been obtained using spatiotemporal complexity derived from resting state activity (Schartner et al. 2015; Schartner et al. 2017; Varley et al. 2020).

The results presented here also speak to functional integration across the network, previously reported to decrease during anesthesia (Schrouff et al. 2011; Luppi et al. 2021), though interestingly not during non-REM sleep (Boly et al. 2012b). This is mostly easily visualized in embedding space, where functional regions tend to move farther apart during states of reduced consciousness (Fig. 5). Decreased functional integration and differentiation during sleep and anesthesia likely play a role in reducing network efficiency during anesthesia and in disorders of consciousness (Monti et al. 2013; Chennu et al. 2014; Hashmi et al. 2017).

We found that changes in D_E were remarkably robust to the choice of frequency band, with comparable results in alpha, beta, and high-gamma bands, and a similar trend in the theta band. D_E measures the complexity of the network organization, and changes in effective dimensionality during sleep and anesthesia reflect changes in that network organization, specifically that locally, brain areas are more tightly coupled and less distinguishable, and globally are less tightly coupled and thus less integrated. The variability of resting state functional connectivity across frequency band during the wake state likely reflects the tendency of different regions of the brain to communicate on different time scales. However, our results show that no matter the time scale that communication is altered in a similar manner by anesthesia and sleep.

A recent study applied DME to BOLD fMRI data to investigate changes in the functional geometry of cortical networks during anesthesia and in unresponsive wakefulness syndrome (Huang et al. 2023). Similar to the results presented here, levels of awareness and wakefulness in that study were related to position of cortical resting state networks in embedding space. Interestingly, Huang and colleagues reported a *decrease* in the range in embedding space that specific networks cover during states of reduced consciousness, suggesting that separate networks are less distinct rather than more distinct as we report here. It is possible that the different measurement modality (iEEG versus fMRI) contributes to this discrepancy because RS iEEG and cerebral blood flow may capture fundamentally different signals in the brain (Maier et al. 2008; Claron et al. 2023). It is also possible that the different analytical approaches emphasized different features of the data and changes in those features during anesthesia and sleep. For example, the D_E measure we employ here estimates the number of dimensions that characterize functional networks in a given brain state. Huang and colleagues instead focus on three particular dimensions that best characterize awake resting state networks and examine how networks in other states map onto those dimensions.

Network transitions during anesthesia and sleep

The dynamics of network transitions are a rich vein of inquiry for understanding the neural basis of consciousness (Golkowski et al. 2019; Huang et al. 2021b). Although these dynamics were not a focus of the current study, the framework presented here readily lends itself to their exploration. For example, simple clustering can distinguish integrated from segregated network states in resting state functional connectivity derived from functional MRI data and enable exploration of the dynamics of state transitions during

resting state and cognitive tasks (Shine et al. 2016; Fukushima et al. 2018). These dynamics are altered under anesthesia, with a shift toward greater time spent in the segregated state and decreases in network complexity and information capacity (Luppi et al. 2019; Luppi et al. 2021).

Although we have divided stages of anesthesia and sleep into two categories, one of reduced consciousness and the other of relatively intact consciousness, this is clearly an oversimplification. These stages of anesthesia (S, U) and sleep are undoubtedly superpositions of the more generally relevant states of unconsciousness, disconnected consciousness (i.e. dreaming), and connected consciousness. Stages of reduced consciousness (U, N2, N3) are likely dominated by segments of unconsciousness, but also include periods of disconnected consciousness (Leslie et al. 2009; Siclari et al. 2013). Similarly, S and N1 are likely mixtures of connected consciousness, disconnected consciousness, and unconsciousness. This continuum is reflected in the smoothly varying changes across stage in D_E and other metrics presented here.

Theories of consciousness

Central to the ongoing debate about the neural correlates of consciousness are their loci in the brain (Boly et al. 2017; Odegaard et al. 2017). Global Neuronal Workspace Theory (Mashour et al. 2020) places prefrontal cortex and its connections with parietal regions central to these correlates, whereas Integrated Information Theory (Tononi et al. 2016) sites these correlates in the "back" of the brain, a region spanning temporal, occipital, and parietal cortex. Although clinical considerations precluded an exhaustive and invariant sampling of brain regions in our cohort of participants, our results indicate that transitions into and out of states of reduced consciousness involve a global network reorganization rather than relying on specific regions (Supplemental Fig. 7). However, observation of global network changes during anesthesia and sleep does not exclude the possibility that local changes in key regions (i.e. prefrontal or parietal cortex) are sufficient to cause LOC. Additionally, even global cortical changes are likely coordinated by small brain areas with broad reach, such as central lateral thalamus (Redinbaugh et al. 2020).

Previous work investigating mechanisms of anesthesia focused on disruptions in connectivity, especially feedback cortico-cortical connectivity. Studies in both human subjects and animal models showed reduced feedback connectivity at doses of anesthetics causing LOC (Boly et al. 2012a; Lee et al. 2013; Raz et al. 2014; Murphy et al. 2019). These data are consistent with the Global Neuronal Workspace Theory, in which feedback from prefrontal cortex to wide areas of the brain is critical for conscious experience, and on a central role for predictive processing in consciousness (Friston 2010; Mashour and Hudetz 2017). However, several findings are not easily reconciled with these models, including reports of increases in connectivity (Murphy et al. 2011; Boly et al. 2012b; Lee et al. 2017b) and the reported suppression of feedforward connectivity (Sanders et al. 2018).

By focusing on network reorganization during states of reduced consciousness, we shift the focus beyond pathway-specific changes during LOC and ROC and explore how local and global changes in connectivity combine to disrupt both differentiation and integration in the unconscious brain. We note that functional integration is not the same as information integration central to Integrated Information Theory, as the latter distinguishes causal from non-causal interactions. Indeed, it is

not possible to ascertain information integration using purely observational data. However, theoretical work has shown that differentiation can be used to establish an upper bound on integrated information (Marshall et al. 2016). Thus, the results presented here, when viewed through the lens of differentiation, are consistent with a decrease in information integration during reduced states of consciousness.

Caveats and limitations

Because participants in the current study had a neurological disorder, results may not generalize to a healthy population. This caveat is inherent to all human intracranial electrophysiology studies, as discussed previously (Banks et al. 2020). However, we note that results presented in this study were consistent across participants with different seizure foci, clinical histories, and drug regimens. It is possible that seizures, ASM use, and the hospital environment may affect sleep and sensitivity to anesthesia. Seizures can disrupt sleep architecture (Touchon et al. 1991; Derry and Duncan 2013; Jain and Kothare 2015), but in the one participant with overnight seizures (L403), data collected after seizures began were excluded. Similarly, although ASMs can alter the structure of sleep (Jain and Glauser 2014), participants had the dosages and number of their ASMs reduced before collection of overnight sleep data. We note that the patients' ASM regimens at the time of sleep and anesthesia data collection varied, and this may have contributed to across-participant variability in results. The quality and structure of sleep may also have been affected by the hospital environment, possibly contributing to the absence of N3 sleep in three participants. Because we had sufficient representation of all studied sleep stages in the cohort (Table 1), the likelihood of entering a particular stage was not a confound. Similarly, while the use of ASMs could lead to a reduction in propofol requirement (Ouchi and Sugiyama 2015), the present study relied on behavioral assessment of arousal. Thus, the definition of stages of anesthesia was not affected by factors secondary to the participants' history of epilepsy.

Future directions

These results contribute to our understanding of the neural correlates of consciousness. Next steps should include recapitulation of these results using scalp EEG, which would enhance the translational relevance of these findings. Assessments in clinical settings often require monitoring of consciousness in real time. Accordingly, tracking the dynamics of D_E and of data in embedding space will enable identification of rapid changes in brain state underlying consciousness transitions. Finally, extending DME analysis to apply to effective connectivity would enable more thorough investigation of causal structure theories of consciousness such as Integrated Information Theory.

Acknowledgments

We are grateful to Haiming Chen, Brian Dlouhy, M. Eric Dyken, Phillip Gander, Christopher Garcia, Timothy Griffiths, Matthew Howard, William Mayner, Christopher Petkov, and Ariane Rhone for help with data collection, analysis, interpretation, and helpful comments on the manuscript.

Supplementary material

Supplementary material is available at *Cerebral Cortex* online.

Author contributions

Bryan Krause (Data curation, Formal analysis, Methodology, Software, Validation, Visualization, Writing—original draft, Writing—review & editing), Declan I. Campbell (Formal analysis, Software, Writing—review & editing), Christopher Kovach (Data curation, Formal analysis, Writing—review & editing), Rashmi Mueller (Investigation, Writing—review & editing), Hiroto Kawasaki (Investigation, Writing—review & editing), Kirill Nourski (Conceptualization, Data curation, Funding acquisition, Investigation, Methodology, Project administration, Supervision, Visualization, Writing—original draft, Writing—review & editing), and Matthew I. Banks (Conceptualization, Formal analysis, Funding acquisition, Investigation, Methodology, Project administration, Supervision, Writing—original draft, Writing—review & editing).

References

Aalling NN, Nedergaard M, DiNuzzo M. Cerebral metabolic changes during sleep. *Curr Neurol Neurosci Rep*. 2018:18(9):57–57.

Akeju O, Brown EN. Neural oscillations demonstrate that general anesthesia and sedative states are neurophysiologically distinct from sleep. *Curr Opin Neurobiol*. 2017:44:178–185.

Alkire MT, Haier RJ, Fallon JH. Toward a unified theory of narcosis: brain imaging evidence for a thalamocortical switch as the neurophysiologic basis of anesthetic- induced unconsciousness. *Conscious Cogn*. 2000:9(3):370–386.

Alkire MT, Hudetz AG, Tononi G. Consciousness and anesthesia. *Science*. 2008:322(5903):876–880.

Banks MI, Krause BM, Endemann CM, Campbell DI, Kovach CK, Dyken ME, Kawasaki H, Nourski KV. Cortical functional connectivity indexes arousal state during sleep and anesthesia. *NeuroImage*. 2020:211:116627.

Banks MI, Krause BM, Berger DG, Campbell DI, Boes AD, Bruss JE, Kovach CK, Kawasaki H, Steinschneider M, Nourski KV. Functional geometry of auditory cortical resting state networks derived from intracranial electrophysiology. *bioRxiv*. 2022: 2022.02.06.479292.

Barttfeld P, Uhrig L, Sitt JD, Sigman M, Jarraya B, Dehaene S. Signature of consciousness in the dynamics of resting-state brain activity. *Proc Natl Acad Sci USA*. 2015:112(3):887–892.

Bastos AM, Usrey WM, Adams RA, Mangun GR, Fries P, Friston KJ. Canonical microcircuits for predictive coding. *Neuron*. 2012:76(4): 695–711.

Bates D, Mächler M, Bolker B, Walker S. Fitting linear mixed-effects models using lme4. *J Stat Softw*. 2015:67(1):48.

Berry RB, Brooks R, Gamaldo CE, Harding SM, Lloyd RM, Marcus CL, Vaughn BV, Medicine FTAAoS. *AASM manual for the scoring of sleep and associated events: rules, terminology and technical specifications, version 2.4*. Darien, IL: American Academy of Sleep Medicine; 2017

Boly M, Moran R, Murphy M, Boveroux P, Bruno MA, Noirhomme Q, Ledoux D, Bonhomme V, Brichant JF, Tononi G, et al. Connectivity changes underlying spectral EEG changes during propofol-induced loss of consciousness. *J Neurosci*. 2012a:32(20): 7082–7090.

Boly M, Perlbarg V, Marrelec G, Schabus M, Laureys S, Doyon J, Pelegrini-Issac M, Maquet P, Benali H. Hierarchical clustering of brain activity during human nonrapid eye movement sleep. *Proc Natl Acad Sci USA*. 2012b:109(15):5856–5861.

Boly M, Massimini M, Tsuchiya N, Postle BR, Koch C, Tononi G. Are the neural correlates of consciousness in the front or in the back of the cerebral cortex? Clinical and neuroimaging evidence. *J Neurosci*. 2017:37(40):9603–9613.

Boveroux P, Vanhaudenhuyse A, Bruno MA, Noirhomme Q, Lauwick S, Luxen A, Degueldre C, Plenevaux A, Schnakers C, Phillips C, et al. Breakdown of within- and between-network resting state functional magnetic resonance imaging connectivity during propofol-induced loss of consciousness. *Anesthesiology*. 2010:113(5):1038–1053.

Caliński T, Harabasz J. A dendrite method for cluster analysis. *Commun Stat*. 1974:3:1–27.

Casali AG, Gosseries O, Rosanova M, Boly M, Sarasso S, Casali KR, Casarotto S, Bruno MA, Laureys S, Tononi G, et al. A theoretically based index of consciousness independent of sensory processing and behavior. *Sci Transl Med*. 2013:5(198):198ra105.

Chennu S, Finoia P, Kamau E, Allanson J, Williams GB, Monti MM, Noreika V, Arnatkeviciute A, Canales-Johnson A, Olivares F, et al. Spectral signatures of reorganised brain networks in disorders of consciousness. *PLoS Comput Biol*. 2014:10(10):e1003887.

Chernik DA, Gillings D, Laine H, Hendler J, Silver JM, Davidson AB, Schwam EM, Siegel JL. Validity and reliability of the Observer's assessment of alertness/sedation scale: study with intravenous midazolam. *J Clin Psychopharmacol*. 1990:10(4): 244–251.

Chiou R, Jefferies E, Duncan J, Humphreys GF, Lambon Ralph MA. A middle ground where executive control meets semantics: the neural substrates of semantic control are topographically sandwiched between the multiple-demand and default-mode systems. *Cereb Cortex*. 2023:33(8):4512–4526.

Claron J, Provansal M, Salardaine Q, Tissier P, Dizeux A, Deffieux T, Picaud S, Tanter M, Arcizet F, Pouget P. Co-variations of cerebral blood volume and single neurons discharge during resting state and visual cognitive tasks in non-human primates. *Cell Rep*. 2023:42(4):112369.

Coifman RR, Hirn MJ. Diffusion maps for changing data. *Appl Comput Harmon Anal*. 2014:36(1):79–107.

Coifman RR, Lafon S, Lee AB, Maggioni M, Nadler B, Warner F, Zucker SW. Geometric diffusions as a tool for harmonic analysis and structure definition of data: diffusion maps. *Proc Natl Acad Sci USA*. 2005:102(21):7426–7431.

Dehaene S, Changeux JP. Experimental and theoretical approaches to conscious processing. *Neuron*. 2011:70(2):200–227.

Del Giudice M. Effective dimensionality: a tutorial. *Multivar Behav Res*. 2021:56(3):527–542.

Derry CP, Duncan S. Sleep and epilepsy. *Epilepsy Behav*. 2013:26(3): 394–404.

Destrieux C, Fischl B, Dale A, Halgren E. Automatic parcellation of human cortical gyri and sulci using standard anatomical nomenclature. *NeuroImage*. 2010:53(1):1–15.

Destrieux C, Terrier LM, Andersson F, Love SA, Cottier JP, Duvernoy H, Velut S, Janot K, Zemmoura I. A practical guide for the identification of major sulcogyral structures of the human cortex. *Brain Struct Funct*. 2017:222(4):2001–2015.

Eer AS, Padmanabhan U, Leslie K. Propofol dose and incidence of dreaming during sedation. *Eur J Anaesthesiol*. 2009:26(10):833–836.

Elvsåshagen T, Mutsaerts HJMM, Zak N, Norbom LB, Quraishi SH, Pedersen PØ, Malt UF, Westlye LT, van Someren EJW, Bjørnerud A, et al. Cerebral blood flow changes after a day of wake, sleep, and sleep deprivation. *NeuroImage*. 2019:186:497–509.

Feinsinger A, Pouratian N, Ebadi H, Adolphs R, Andersen R, Beauchamp MS, Chang EF, Crone NE, Collinger JL, Fried I, et al. Ethical commitments, principles, and practices guiding intracranial neuroscientific research in humans. *Neuron*. 2022:110(2): 188–194.

Ferrarelli F, Massimini M, Sarasso S, Casali A, Riedner BA, Angelini G, Tononi G, Pearce RA. Breakdown in cortical effective connectivity during midazolam-induced loss of consciousness. *Proc Natl Acad Sci USA*. 2010:107(6):2681–2686.

Friston K. The free-energy principle: a unified brain theory? *Nat Rev Neurosci*. 2010:11(2):127–138.

Fukushima M, Betzel RF, He Y, van den Heuvel MP, Zuo XN, Sporns O. Structure-function relationships during segregated and integrated network states of human brain functional connectivity. *Brain Struct Funct*. 2018:223(3):1091–1106.

Gan TJ, Glass PS, Windsor A, Payne F, Rosow C, Sebel P, Manberg P. Bispectral index monitoring allows faster emergence and improved recovery from propofol, alfentanil, and nitrous oxide anesthesia. BIS utility study group. *Anesthesiology*. 1997:87(4): 808–815.

Golkowski D, Larroque SK, Vanhaudenhuyse A, Plenevaux A, Boly M, Di Perri C, Ranft A, Schneider G, Laureys S, Jordan D, et al. Changes in whole brain dynamics and connectivity patterns during Sevoflurane- and Propofol-induced unconsciousness identified by functional magnetic resonance imaging. *Anesthesiology*. 2019:130(6):898–911.

Hacker CD, Snyder AZ, Pahwa M, Corbetta M, Leuthardt EC. Frequency-specific electrophysiologic correlates of resting state fMRI networks. *NeuroImage*. 2017:149:446–457.

Hashmi JA, Loggia ML, Khan S, Gao L, Kim J, Napadow V, Brown EN, Akeju O. Dexmedetomidine disrupts the local and global efficiencies of large-scale brain networks. *Anesthesiology*. 2017:126(3): 419–430.

Hipp JF, Hawellek DJ, Corbetta M, Siegel M, Engel AK. Large-scale cortical correlation structure of spontaneous oscillatory activity. *Nat Neurosci*. 2012:15(6):884–890.

Hong SJ, Vos de Wael R, Bethlehem RAI, Lariviere S, Paquola C, Valk SL, Milham MP, Di Martino A, Margulies DS, Smallwood J, et al. Atypical functional connectome hierarchy in autism. *Nat Commun*. 2019:10(1):1022.

Huang Z, Tarnal V, Vlisides PE, Janke EL, McKinney AM, Picton P, Mashour GA, Hudetz AG. Anterior insula regulates brain network transitions that gate conscious access. *Cell Rep*. 2021a:35(5):109081.

Huang Z, Tarnal V, Vlisides PE, Janke EL, McKinney AM, Picton P, Mashour GA, Hudetz AG. Asymmetric neural dynamics characterize loss and recovery of consciousness. *NeuroImage*. 2021b:236:118042.

Huang Z, Mashour GA, Hudetz AG. Functional geometry of the cortex encodes dimensions of consciousness. *Nat Commun*. 2023:14(1):72.

Hudetz AG. General anesthesia and human brain connectivity. *Brain Connect*. 2012:2(6):291–302.

Hudetz AG, Humphries CJ, Binder JR. Spin-glass model predicts metastable brain states that diminish in anesthesia. *Front Syst Neurosci*. 2014:8:234.

Hutchison RM, Hutchison M, Manning KY, Menon RS, Everling S. Isoflurane induces dose-dependent alterations in the cortical connectivity profiles and dynamic properties of the brain's functional architecture. *Hum Brain Mapp*. 2014:35(12):5754–5775.

Jain SV, Glauser TA. Effects of epilepsy treatments on sleep architecture and daytime sleepiness: an evidence-based review of objective sleep metrics. *Epilepsia*. 2014:55(1):26–37.

Jain SV, Kothare SV. Sleep and epilepsy. *Semin Pediatr Neurol*. 2015:22(2):86–92.

Jenkinson M, Bannister P, Brady M, Smith S. Improved optimization for the robust and accurate linear registration and motion correction of brain images. *NeuroImage*. 2002:17(2):825–841.

Katsumi Y, Zhang J, Chen D, Kamona N, Bunce JG, Hutchinson JB, Yarossi M, Tunik E, Dickerson BC, Quigley KS, et al. Correspondence of functional connectivity gradients across human isocortex, cerebellum, and hippocampus. *Commun Biol*. 2023:6(1):401.

Kovach CK, Gander PE. The demodulated band transform. *J Neurosci Methods*. 2016:261:135–154.

Langs G, Golland P, Tie Y, Rigolo L, Golby AJ. Functional geometry alignment and localization of brain areas. *Adv Neural Inf Process Syst*. 2010:1:1225–1233.

Lee U, Oh G, Kim S, Noh G, Choi B, Mashour GA. Brain networks maintain a scale-free organization across consciousness, anesthesia, and recovery: evidence for adaptive reconfiguration. *Anesthesiology*. 2010:113(5):1081–1091.

Lee U, Ku S, Noh G, Baek S, Choi B, Mashour GA. Disruption of frontal-parietal communication by ketamine, propofol, and sevoflurane. *Anesthesiology*. 2013:118(6):1264–1275.

Lee H, Noh GJ, Joo P, Choi BM, Silverstein BH, Kim M, Wang J, Jung WS, Kim S. Diversity of functional connectivity patterns is reduced in propofol-induced unconsciousness. *Hum Brain Mapp*. 2017a:38(10):4980–4995.

Lee M, Sanders RD, Yeom SK, Won DO, Seo KS, Kim HJ, Tononi G, Lee SW. Network properties in transitions of consciousness during propofol-induced sedation. *Sci Rep*. 2017b:7(1):16791.

Lenth RV. *Emmeans: estimated marginal means, aka least-squares means*; 2019 R package version 1.3.3. https://cran.r-project.org/web/packages/emmeans/.

Leski S, Linden H, Tetzlaff T, Pettersen KH, Einevoll GT. Frequency dependence of signal power and spatial reach of the local field potential. *PLoS Comput Biol*. 2013:9(7):e1003137.

Leslie K, Sleigh J, Paech MJ, Voss L, Lim CW, Sleigh C. Dreaming and electroencephalographic changes during anesthesia maintained with propofol or desflurane. *Anesthesiology*. 2009:111(3):547–555.

Li Y, Wang S, Pan C, Xue F, Xian J, Huang Y, Wang X, Li T, He H. Comparison of NREM sleep and intravenous sedation through local information processing and whole brain network to explore the mechanism of general anesthesia. *PLoS One*. 2018:13(2):e0192358.

Liu ZQ, Betzel RF, Misic B. Benchmarking functional connectivity by the structure and geometry of the human brain. *Netw Neurosci*. 2022:6(4):937–949.

Luppi AI, Craig MM, Pappas I, Finoia P, Williams GB, Allanson J, Pickard JD, Owen AM, Naci L, Menon DK, et al. Consciousness-specific dynamic interactions of brain integration and functional diversity. *Nat Commun*. 2019:10(1):4616.

Luppi AI, Golkowski D, Ranft A, Ilg R, Jordan D, Menon DK, Stamatakis EA. Brain network integration dynamics are associated with loss and recovery of consciousness induced by sevoflurane. *Hum Brain Mapp*. 2021:42(9):2802–2822.

Maier A, Wilke M, Aura C, Zhu C, Ye FQ, Leopold DA. Divergence of fMRI and neural signals in V1 during perceptual suppression in the awake monkey. *Nat Neurosci*. 2008:11(10):1193–1200.

Margulies DS, Ghosh SS, Goulas A, Falkiewicz M, Huntenburg JM, Langs G, Bezgin G, Eickhoff SB, Castellanos FX, Petrides M, et al. Situating the default-mode network along a principal gradient of macroscale cortical organization. *Proc Natl Acad Sci USA*. 2016:113(44):12574–12579.

Marshall W, Gomez-Ramirez J, Tononi G. Integrated information and state differentiation. *Front Psychol*. 2016:7:926. https://doi.org/10.3389/fpsyg.2016.00926.

Mashour GA. Top-down mechanisms of anesthetic-induced unconsciousness. *Front Syst Neurosci*. 2014:8:115.

Mashour GA, Hudetz AG. Bottom-up and top-down mechanisms of general anesthetics modulate different dimensions of consciousness. *Front Neural Circuits*. 2017:11:44.

Mashour GA, Hudetz AG. Neural correlates of unconsciousness in large-scale brain networks. *Trends Neurosci*. 2018:41(3):150–160.

Mashour GA, Roelfsema P, Changeux JP, Dehaene S. Conscious processing and the global neuronal workspace hypothesis. *Neuron*. 2020:105(5):776–798.

Massimini M, Ferrarelli F, Huber R, Esser SK, Singh H, Tononi G. Breakdown of cortical effective connectivity during sleep. *Science*. 2005:309(5744):2228–2232.

Meng Y, Yang S, Xiao J, Lu Y, Li J, Chen H, Liao W. Cortical gradient of a human functional similarity network captured by the geometry of cytoarchitectonic organization. *Commun Biol*. 2022:5(1):1152.

Monti MM, Lutkenhoff ES, Rubinov M, Boveroux P, Vanhaudenhuyse A, Gosseries O, Bruno MA, Noirhomme Q, Boly M, Laureys S. Dynamic change of global and local information processing in propofol-induced loss and recovery of consciousness. *PLoS Comput Biol*. 2013:9(10):e1003271.

Murphy M, Bruno MA, Riedner BA, Boveroux P, Noirhomme Q, Landsness EC, Brichant JF, Phillips C, Massimini M, Laureys S, et al. Propofol anesthesia and sleep: a high-density EEG study. *Sleep*. 2011:34(3):283–291.

Murphy C, Krause B, Banks M. Selective effects of isoflurane on cortico-cortical feedback afferent responses in murine non-primary neocortex. *Br J Anaesth*. 2019:123(4):488–496.

Nourski KV, Howard MA 3rd. Invasive recordings in the human auditory cortex. *Handb Clin Neurol*. 2015:129:225–244.

Nourski KV, Steinschneider M, Rhone AE, Kawasaki H, Howard MA 3rd, Banks MI. Auditory predictive coding across awareness states under Anesthesia: an intracranial electrophysiology study. *J Neurosci*. 2018:38(39):8441–8452.

Nourski KV, Steinschneider M, Rhone AE, Mueller RN, Kawasaki H, Banks MI. Arousal state-dependence of interactions between short- and long-term auditory novelty responses in human subjects. *Front Hum Neurosci*. 2021:15:737230.

Odegaard B, Knight RT, Lau H. Should a few null findings falsify prefrontal theories of conscious perception? *J Neurosci*. 2017:37(40):9593–9602.

Oldehinkel M, Tiego J, Sabaroedin K, Chopra S, Francey SM, O'Donoghue B, Cropley V, Nelson B, Graham J, Baldwin L, et al. Gradients of striatal function in antipsychotic-free first-episode psychosis and schizotypy. *Transl Psychiatry*. 2023:13(1):128.

Ouchi K, Sugiyama K. Required propofol dose for anesthesia and time to emerge are affected by the use of antiepileptics: prospective cohort study. *BMC Anesthesiol*. 2015:15(1):34.

Palanca BJ, Mitra A, Larson-Prior L, Snyder AZ, Avidan MS, Raichle ME. Resting-state functional magnetic resonance imaging correlates of Sevoflurane-induced unconsciousness. *Anesthesiology*. 2015:123(2):346–356.

Parkes L, Kim JZ, Stiso J, Calkins ME, Cieslak M, Gur RE, Gur RC, Moore TM, Ouellet M, Roalf DR, et al. Asymmetric signaling across the hierarchy of cytoarchitecture within the human connectome. *Sci Adv*. 2022:8(50):eadd2185.

Picchioni D, Pixa ML, Fukunaga M, Carr WS, Horovitz SG, Braun AR, Duyn JH. Decreased connectivity between the thalamus and the

neocortex during human nonrapid eye movement sleep. *Sleep.* 2014:37(2):387–397.

Pines A, Keller AS, Larsen B, Bertolero M, Ashourvan A, Bassett DS, Cieslak M, Covitz S, Fan Y, Feczko E, et al. Development of top-down cortical propagations in youth. *Neuron*. 2023:111(8): 1316–1330.e5.

Ranft A, Golkowski D, Kiel T, Riedl V, Kohl P, Rohrer G, Pientka J, Berger S, Thul A, Maurer M, et al. Neural correlates of Sevoflurane-induced unconsciousness identified by simultaneous functional magnetic resonance imaging and electroencephalography. *Anesthesiology*. 2016:125(5):861–872.

Raz A, Grady SM, Krause BM, Uhlrich DJ, Manning KA, Banks MI. Preferential effect of isoflurane on top-down versus bottom-up pathways in sensory cortex. *Front Syst Neurosci*. 2014:8:191. https://doi.org/10.3389/fnsys.2014.00191.

Redinbaugh MJ, Phillips JM, Kambi NA, Mohanta S, Andryk S, Dooley GL, Afrasiabi M, Raz A, Saalmann YB. Thalamus modulates consciousness via layer-specific control of cortex. *Neuron*. 2020:106(1):66–75.e12.

Rohr K, Stiehl HS, Sprengel R, Buzug TM, Weese J, Kuhn MH. Landmark-based elastic registration using approximating thin-plate splines. *IEEE Trans Med Imaging*. 2001:20(6):526–534.

Sanders RD, Banks MI, Darracq M, Moran R, Sleigh J, Gosseries O, Bonhomme V, Brichant JF, Rosanova M, Raz A, et al. Propofol-induced unresponsiveness is associated with impaired feedforward connectivity in cortical hierarchy. *Br J Anaesth*. 2018:121(5): 1084–1096.

Sarasso S, Boly M, Napolitani M, Gosseries O, Charland-Verville V, Casarotto S, Rosanova M, Casali AG, Brichant JF, Boveroux P, et al. Consciousness and complexity during unresponsiveness induced by Propofol, xenon, and ketamine. *Curr Biol*. 2015:25(23): 3099–3105.

Sarasso S, Casali AG, Casarotto S, Rosanova M, Sinigaglia C, Massimini M. Consciousness and complexity: a consilience of evidence. *Neurosci Consciousness*. 2021:7(2):1–24.

Satopaa V, Albrecht J, Irwin D, Raghavan B editors. Finding a "Kneedle" in a haystack: Detecting knee points in system behavior, *2011 31st International Conference on Distributed Computing Systems Workshops*, 20–24 June 2011, 2011, pp. 166–171

Schartner M, Seth A, Noirhomme Q, Boly M, Bruno MA, Laureys S, Barrett A. Complexity of multi-dimensional spontaneous EEG decreases during propofol induced general anaesthesia. *PLoS One*. 2015:10(8):e0133532.

Schartner MM, Pigorini A, Gibbs SA, Arnulfo G, Sarasso S, Barnett L, Nobili L, Massimini M, Seth AK, Barrett AB. Global and local complexity of intracranial EEG decreases during NREM sleep. *Neurosci Consciousness*. 2017:2017:niw022.

Scheinin A, Kantonen O, Alkire M, Langsjo J, Kallionpaa RE, Kaisti K, Radek L, Johansson J, Sandman N, Nyman M, et al. Foundations of human consciousness: imaging the twilight zone. *J Neurosci*. 2021:41(8):1769–1778.

Schrouff J, Perlbarg V, Boly M, Marrelec G, Boveroux P, Vanhaudenhuyse A, Bruno MA, Laureys S, Phillips C, Pelegrini-Issac M, et al. Brain functional integration decreases during propofol-induced loss of consciousness. *NeuroImage*. 2011:57(1):198–205.

Shine JM, Bissett PG, Bell PT, Koyejo O, Balsters JH, Gorgolewski KJ, Moodie CA, Poldrack RA. The dynamics of functional brain networks: integrated network states during cognitive task performance. *Neuron*. 2016:92(2):544–554.

Siclari F, Larocque JJ, Postle BR, Tononi G. Assessing sleep consciousness within subjects using a serial awakening paradigm. *Front Psychol*. 2013:4:542.

Sleigh J, Warnaby C, Tracey I. General anaesthesia as fragmentation of selfhood: insights from electroencephalography and neuroimaging. *Br J Anaesth*. 2018:121(1):233–240.

Spoormaker VI, Schroter MS, Gleiser PM, Andrade KC, Dresler M, Wehrle R, Samann PG, Czisch M. Development of a large-scale functional brain network during human non-rapid eye movement sleep. *J Neurosci*. 2010:30(34):11379–11387.

Timmermann C, Roseman L, Haridas S, Rosas FE, Luan L, Kettner H, Martell J, Erritzoe D, Tagliazucchi E, Pallavicini C, et al. Human brain effects of DMT assessed via EEG-fMRI. *Proc Natl Acad Sci USA*. 2023:120(13):e2218949120.

Tononi G, Boly M, Massimini M, Koch C. Integrated information theory: from consciousness to its physical substrate. *Nat Rev Neurosci*. 2016:17(7):450–461.

Touchon J, Baldy-Moulinier M, Billiard M, Besset A, Cadilhac J. Sleep organization and epilepsy. *Epilepsy Res Suppl*. 1991:2:73–81.

Varley TF, Luppi AI, Pappas I, Naci L, Adapa R, Owen AM, Menon DK, Stamatakis EA. Consciousness & Brain Functional Complexity in Propofol anaesthesia. *Sci Rep*. 2020:10(1):1018.

Wang S, Li Y, Qiu S, Zhang C, Wang G, Xian J, Li T, He H. Reorganization of rich-clubs in functional brain networks during propofol-induced unconsciousness and natural sleep. *Neuroimage Clin*. 2020:25:102188.

Yang C, Zhang W, Liu J, Yao L, Bishop JR, Lencer R, Gong Q, Yang Z, Lui S. Disrupted subcortical functional connectome gradient in drug-naïve first-episode schizophrenia and the normalization effects after antipsychotic treatment. *Neuropsychopharmacology*. 2023:48(5):789–796.